A HWENO reconstruction based high-order compact gas-kinetic scheme on unstructured mesh

Xing Ji [a], Fengxiang Zhao [b], Wei Shyy [b], Kun Xu [a,b,c,*]

[a] Department of Mathematics, Hong Kong University of Science and Technology, Clear Water Bay, Kowloon, Hong Kong
[b] Department of Mechanical and Aerospace Engineering, Hong Kong University of Science and Technology, Clear Water Bay, Kowloon, Hong Kong
[c] Shenzhen Research Institute, Hong Kong University of Science and Technology, Shenzhen, China

ARTICLE INFO

ABSTRACT

As an extension of a fourth-order compact gas kinetic scheme (GKS) on structured mesh [24], this work is about the development of a third-order compact GKS on unstructured mesh for the compressible Euler and Navier-Stokes solutions. Based on the time accurate high-order gas-kinetic evolution solution, the time-dependent gas distribution function at a cell interface in GKS provides not only the flux function and its time derivative, but also the time accurate flow variables there at the next time level. As a result, besides updating the conservative flow variables inside each control volume through the interface fluxes, the cell averaged first-order spatial derivatives of flow variables can be obtained as well using the updated flow variables at the closed cell interfaces around that cell through the divergence theorem. Therefore, with the cell-averaged flow variables and their first-order spatial derivatives inside each cell, the Hermite WENO (HWENO) techniques can be naturally implemented for the compact high-order reconstruction at the beginning of the next time step. Following the reconstruction technique in [64], a new HWENO reconstruction on triangular mesh is designed in the current scheme. Combined with the two-stage temporal discretization and second-order time accurate flux function, a third-order compact scheme on unstructured mesh has been constructed. Accurate solutions can be obtained for both inviscid and viscous flows without sensitive dependence on the quality of triangular mesh. The robustness and accuracy of the scheme have been validated through many cases, including strong shocks in the hypersonic viscous flow and smooth Navier-Stokes solution.

© 2020 Elsevier Inc. All rights reserved.

1. Introduction

In computational fluid dynamics (CFD) applications with complex geometry, the unstructured mesh is widely used due to its flexible adaptability. In such a mesh, many techniques used on structured mesh cannot be directly extended here. For example, the third-order WENO method [21] on unstructured mesh needs many neighboring cells in the reconstruction, and the number of cells used in the reconstruction may not be fixed. Theoretically, for a non-compact scheme a large disparity between the numerical domain of dependence and the physical domain of dependence indicates the intrinsic weakness in

either physical model or the numerical discretization [57]. Thus, it is preferred to design a compact high-order scheme, which connects the target cell with its closest neighbors, and to use a CFL number as large as possible. Great effort has been paid on the development of compact schemes in the past decades [51]. Two main representatives of compact schemes are the Discontinuous Galerkin (DG) method [9] and correction procedure via reconstruction (CPR) [59], which are attractive because of their compactness and large number of flops per memory reference. However, they have restricted CFL number in the determination of time step. Most of those methods use Riemann solvers or approximate Riemann solvers for the flux evaluation, and adopt the Runge-Kutta time-stepping method for the time accuracy. Based on the time-dependent gas-kinetic flux function [55], the corresponding schemes under the DG and CPR frameworks have also been developed with triangular mesh [36,60]. But, the advantages of GKS have not been fully utilized in the above approaches, at least the time step has not been enlarged in comparison with Riemann solver based DG methods.

Higher than second-order gas kinetic schemes (HGKS) have been developed systematically in the past decades [31]. In comparison with traditional Riemann solver based high-order CFD methods, the distinguishable points of HGKS include the following: (i) The time-dependent gas distribution function at a cell interface provides a multiple scale flow physics from the kinetic particle transport to the hydrodynamic wave propagation, which bridges the evolution from the kinetic flux vector splitting (KFVS) to the central difference Lax-Wendroff type discretization. (ii) Both inviscid and viscous fluxes are obtained from the moments of a single gas distribution function. (iii) The GKS is a multi-dimensional scheme [58], where both normal and tangential derivatives of flow variables around a cell interface participate in the time evolution of the gas distribution function. (iv) Besides fluxes, the time-dependent gas distribution function at a cell interface also provides time-evolving flow variables at the cell interface, which can be used to construct compact schemes. The first high-order GKS is the one-stage third-order scheme with a third-order time accurate flux function [39,31]. In this scheme, both cell averaged and cell interface flow variables are directly implemented in the reconstruction. The one-step time-stepping formulation and the rigid use of interface values make the scheme be complex and lack of robustness.

Recently, with the incorporation of multi-stage multi-derivative (MSMD) technique, a family of HGKS has been developed [26]. Based on the fifth-order WENO reconstruction [27,2], the performance of HGKS shows great advantages in terms of efficiency, accuracy, and robustness in comparison with traditional high-order schemes with Riemann solver, especially in the capturing of shear instabilities due to its multi-dimensionality in the GKS flux function. Among the MSMD GKS, the two-stage fourth-order (S2O4) GKS [41] seems to be an optimal choice in practical CFD computations. The S2O4 GKS is both efficient and accurate, and as robust as the second-order GKS. With the evaluation of cell averaged slopes from the cell interface values, the adoption of the two-stage time discretization, and compact Hermite WENO (HWENO) reconstruction [43], a class of compact GKS with the spatial accuracy from fifth-order to eighth-order on two-dimensional structured mesh has been developed [24,61]. The fifth-order compact scheme [24] can take a CFL number around 0.5, and it shows better performance than the same order and the same stencils based DG method in all aspects of efficiency, robustness, and accuracy in the compressible viscous flow simulations with shocks. The sixth- and eighth-order compact scheme [61] can achieve a spectral-like resolution at large wavenumber and give great advantages in both tracking the linear aero-acoustic wave and capturing shock-shock interactions. As a continuation, here we further extend the compact two-stage GKS to unstructured mesh.

In any high-order scheme, the reconstruction plays an important role. The WENO-type reconstruction achieves great success [27,2,43,29], especially for the high speed flow with discontinuities. The coefficients for the reconstruction are solely geometric dependence, which can be pre-determined in the computation. The limiting process depends on the non-linear weights. The classical WENO techniques are based on the reconstructions from both low-order sub-stencils to high-order large stencils [27,2,43], which are very effective on structured mesh. The similar idea has been used in the construction of third-order compact HWENO on unstructured triangular mesh [21,63]. The direct applications of the reconstruction from the structured case to the unstructured one meet the following problems. Firstly, the linear combinations of the point values from six sub-stencils in [63] cannot exactly recover the corresponding values from large stencils in smooth cases, where at least eight sub-stencils are required [21]. Secondly, in general the linear weights are not all positive and some linear weights could take very large values, which subsequently distort the numerical solutions. Some techniques have been used to resolve these problems for non-compact WENO reconstruction [62], but they cannot be directly extended to HWENO reconstruction. To overcome these difficulties, Zhu et al. [64] designed a new type of WENO reconstruction on triangular mesh for finite volume method. The key idea is that the WENO procedure is performed on the whole polynomials rather than at each Gaussian point. The linear weights can be chosen to be any positive number as long as the summation goes to one, and the scheme keeps the expected order of accuracy in smooth region. The smooth indicators are carefully designed to achieve such a goal. In addition, the number of sub-stencils can be reduced in this method. Therefore, in this paper we are going to design a new compact third-order HWENO reconstruction by following the similar idea. A quadratic polynomial is constructed first from a total of 10 available cell averaged flow variables and their slopes within the compact stencils. Each of the three sub-stencils is composed of three cells with averaged values.

In this paper, combining the second-order gas kinetic flux function and the two-stage temporal discretization, a new compact third-order GKS will be proposed. The compact scheme inherits the advantages of original two-stage GKS [41,24]. It allows a larger CFL number than the same-order DG method. Compared with the third-order Runge Kutta (RK) time stepping method, it achieves a third-order accuracy in time with one middle stage only. At the same time, benefiting from the newly designed HWENO reconstruction, the compact scheme has less number of sub-stencils than the previous method [63], resulting in an improvement in efficiency. More importantly, the current scheme demonstrates excellent robustness

in the test cases with strong shocks, such as the hypersonic flow passing a cylinder up to Mach number 20. From the perspective of programming, the current code can be easily developed under a finite volume framework, which has the same advantages as the reconstructed-DG (RDG)/PnPm method [35,12]. But, different from the RDG method, the slopes within a cell in the current scheme are updated by the time accurate solutions as Gaussian points along cell interfaces through the Green-Gauss theorem, rather than by the evolution solution of the slopes directly. The different slope update makes fundamental differences between the current compact GKS and other DG methods in terms of the use of large time step and robustness in capturing discontinuous solution.

This paper is organized as follows. In Section 2, a brief review of finite volume GKS on triangular mesh is presented. The general formulation for the two-stage temporal discretization is introduced in Section 3. In Section 4, the compact third-order HWENO reconstruction on triangular mesh is presented. Section 5 includes inviscid and viscous test cases. The last section is the conclusion.

2. Finite volume gas-kinetic scheme

2.1. Finite volume scheme on unstructured mesh

The two-dimensional gas-kinetic BGK equation [1] can be written as

$$f_t + \mathbf{u} \cdot \nabla f = \frac{g - f}{\tau}, \tag{1}$$

where f is the gas distribution function, g is the corresponding equilibrium state, and τ is the collision time. The collision term satisfies the following compatibility condition

$$\int \frac{g - f}{\tau} \psi \mathrm{d}\Xi = 0, \tag{2}$$

where $\psi = (1, u, v, \frac{1}{2}(u^2 + v^2 + \xi^2))^T$, $\mathrm{d}\Xi = \mathrm{d}u\mathrm{d}v\mathrm{d}\xi_1...\mathrm{d}\xi_K$, K is the number of internal degree of freedom, i.e. $K = (4 - 2\gamma)/(\gamma - 1)$ for two-dimensional flows, and γ is the specific heat ratio.

Based on the Chapman-Enskog expansion for BGK equation [56], the gas distribution function in the continuum regime can be expanded as

$$f = g - \tau D_{\mathbf{u}} g + \tau D_{\mathbf{u}}(\tau D_{\mathbf{u}}) g - \tau D_{\mathbf{u}}[\tau D_{\mathbf{u}}(\tau D_{\mathbf{u}}) g] + ...,$$

where $D_{\mathbf{u}} = \partial/\partial t + \mathbf{u} \cdot \nabla$. By truncating on different orders of τ, the corresponding macroscopic equations can be derived. For the Euler equations, the zeroth-order truncation is taken, i.e. $f = g$. For the Navier-Stokes equations, the first-order truncated distribution function is

$$f = g - \tau (u g_x + v g_y + g_t).$$

For a polygon cell Ω_i, the boundary can be expressed as

$$\partial \Omega_i = \bigcup_{p=1}^{m} \Gamma_{ip},$$

where m is the number of cell interfaces for cell Ω_i, which has $m = 3$ for a triangular mesh. Taking moments of the BGK equation (1) and integrating over the cell Ω_i, the semi-discretized form of finite volume scheme can be written as

$$\frac{\mathrm{d}W_i}{\mathrm{d}t} = \mathcal{L}(W_i) = -\frac{1}{|\Omega_i|} \sum_{p=1}^{m} \oint_{\Gamma_{ip}} \mathbf{F}(W) \cdot \mathbf{n}_p \mathrm{d}s, \tag{3}$$

where W_i is the cell averaged value over cell Ω_i, $|\Omega_i|$ is the area of Ω_i, $\mathcal{L}(W)$ is the spatial operator of flux, $\mathbf{F} = (F, G)^T$ and $\mathbf{n}_p$ is the outer normal direction of Γ_{ip}.

In this paper, a third-order spatial reconstruction will be introduced, and the line integral over Γ_{ip} is discretized according to Gaussian quadrature as follows

$$\oint_{\Gamma_{ip}} \mathbf{F}(W) \cdot \mathbf{n}_p \mathrm{d}s = |l_p| \sum_{k=1}^{2} \omega_k \mathbf{F}(\mathbf{x}_{p,k}, t) \cdot \mathbf{n}_p, \tag{4}$$

where $|l_p|$ is the length of the cell interface Γ_{ip}, $\omega_1 = \omega_2 = 1/2$ are the Gaussian quadrature weights, and the Gaussian points $\mathbf{x}_{p,k}, k = 1, 2$ for Γ_{ip} are defined as

$$\mathbf{x}_{p1} = \frac{3 + \sqrt{3}}{6}\mathbf{X}_{p1} + \frac{3 - \sqrt{3}}{6}\mathbf{X}_{p2}, \ \mathbf{x}_{p2} = \frac{3 + \sqrt{3}}{6}\mathbf{X}_{p2} + \frac{3 - \sqrt{3}}{6}\mathbf{X}_{p1},$$

where $\mathbf{X}_{p1}, \mathbf{X}_{p2}$ are the endpoints of Γ_{ip}.

The fluxes in unit length across each Gaussian point for the updates of flow variables in a global coordinate can be written as follows

$$\mathbf{F}(\mathbf{x}_{p,k}, t) \cdot \mathbf{n}_p = \int \psi f(x_{p,k}, y_{p,k}, t, u, v, \xi) \mathbf{u} \cdot \mathbf{n} du dv d\xi, \tag{5}$$

where $f(x_{p,k}, y_{p,k}, t, u, v, \xi)$ is the gas distribution function at the corresponding Gaussian point. Here we can first evaluate the fluxes in a local coordinate

$$\tilde{F}_{p,k}(t) = \int \psi \tilde{u} f(\tilde{x}_{p,k}, \tilde{y}_{p,k}, t, \tilde{u}, \tilde{v}, \xi) d\tilde{u} d\tilde{v} d\xi,$$

where the original point of the local coordinate is $(\tilde{x}_{p,k}, \tilde{y}_{p,k}) = (0, 0)$ with x-direction in $\mathbf{n}_p$. Then the velocities in the local coordinate are given by

$$\begin{cases} \tilde{u} = u \cos\theta + v \sin\theta, \\ \tilde{v} = -u \sin\theta + v \cos\theta. \end{cases}$$

In 2-D case, the global and local fluxes are related as [39]

$$\mathbf{F}(W) \cdot \mathbf{n} = F(W) \cos\theta + G(W) \sin\theta = T^{-1} F(TW),$$

where $T = T(\theta)$ is the rotation matrix

$$T = \begin{pmatrix} 1 & 0 & 0 & 0 \\ 0 & \cos\theta & \sin\theta & 0 \\ 0 & -\sin\theta & \cos\theta & 0 \\ 0 & 0 & 0 & 1 \end{pmatrix}.$$

2.2. Second-order gas-kinetic flux solver

The formulation of gas kinetic flux will be presented in a local coordinate. We omit the tilde on flow variables for simplicity. In order to construct the numerical fluxes, the integral solution of BGK equation (1) is used

$$f(x_{p,k}, y_{p,k}, t, u, v, \xi) = \frac{1}{\tau} \int_0^t g(x', y', t', u, v, \xi) e^{-(t-t')/\tau} dt' + e^{-t/\tau} f_0(-ut, -vt, u, v, \xi), \tag{6}$$

where $(x_{p,k}, y_{p,k}) = (0, 0)$ is the quadrature point of a cell interface in the local coordinate, and $x_{p,k} = x' + u(t - t')$ and $y_{p,k} = y' + v(t - t')$ are the trajectory of particles. f_0 is the initial gas distribution function and g is the corresponding equilibrium state. The flow dynamics at a cell interface depends on the ratio of time step to the local particle collision time $\Delta t/\tau$, which covers an evolution process from the particle free transport of f_0 to equilibrium state of g.

To construct a time evolution solution of the gas distribution function at a cell interface, the following notations are introduced first

$$a_1 = (\partial g/\partial x)/g, a_2 = (\partial g/\partial y)/g, A = (\partial g/\partial t)/g,$$

where g is the equilibrium state. The variables (a_1, a_2, A), denoted by ω, depend on particle velocities in the form of [55]

$$\omega = \omega_1 + \omega_2 u + \omega_3 v + \omega_4 \frac{1}{2}(u^2 + v^2 + \xi^2).$$

For the kinetic part of the integral solution Eq. (6), the initial gas distribution function is constructed as

$$f_0 = f_0^l(x, y, u, v)\mathbb{H}(x) + f_0^r(x, y, u, v)(1 - \mathbb{H}(x)),$$

where $\mathbb{H}(x)$ is the Heaviside function. Here f_0^l and f_0^r are the initial gas distribution functions on both sides of a cell interface, which have one to one correspondence with the initially reconstructed macroscopic variables. For the second-order scheme, the Taylor expansion for the gas distribution function in space around $(x, y) = (0, 0)$ is expressed as

$$f_0^k(x, y) = f_G^k(0, 0) + \frac{\partial f_G^k}{\partial x}x + \frac{\partial f_G^k}{\partial y}y, \tag{7}$$

for $k = l, r$. According to the Chapman-Enskog expansion, f_G^k has the form

$$f_G^k = g_k - \tau(a_{1k}u + a_{2k}v + A_k)g_k, \tag{8}$$

where g_l, g_r are the equilibrium states which can be fully determined from the reconstructed macroscopic variables W_l, W_r at the left and right sides of a cell interface. Substituting Eq. (7) and Eq. (8) into Eq. (6), the kinetic part in the integral solution can be written as

$$e^{-t/\tau} f_0^k(-ut, -vt, u, v, \xi) = e^{-t/\tau} g_k[1 - \tau(a_{1k}u + a_{2k}v + A_k) - t(a_{1k}u + a_{2k}v)], \tag{9}$$

where the coefficients $a_{1k}, ..., A_k, k = l, r$ are defined according to the expansion of g_k. After determining the kinetic part f_0, the equilibrium state g in the integral solution Eq. (6) can be expanded in space and time as follows

$$g = g_0 + \frac{\partial g_0}{\partial x}x + \frac{\partial g_0}{\partial y}y + \frac{\partial g_0}{\partial t}t, \tag{10}$$

where g_0 is the equilibrium state located at an interface, which can be determined through the compatibility condition Eq. (2),

$$\int \psi g_0 d\Xi = W_0 = \int_{u>0} \psi g_l d\Xi + \int_{u<0} \psi g_r d\Xi, \tag{11}$$

where W_0 are the macroscopic flow variables for the determination of the equilibrium state g_0. Substituting Eq. (10) into Eq. (6), the hydrodynamic part in the integral solution can be written as

$$\frac{1}{\tau} \int_0^t g(x', y', t', u, v, \xi)e^{-(t-t')/\tau}dt' = C_1 g_0 + C_2 g_0(\bar{a}_1 u + \bar{a}_2 v) + C_3 g_0 \bar{A}, \tag{12}$$

where the coefficients $\bar{a}_1, \bar{a}_2, ..., \bar{A}$ are defined from the expansion of the equilibrium state g_0. The coefficients $C_i, i = 1, 2, 3$ in Eq. (12) are given by

$$C_1 = 1 - e^{-t/\tau}, C_2 = (t + \tau)e^{-t/\tau} - \tau, C_3 = t - \tau + \tau e^{-t/\tau}.$$

The coefficients in Eq. (9) and Eq. (12) can be determined by the spatial derivatives of macroscopic flow variables and the compatibility condition as follows

$$\langle a_1 \rangle = \frac{\partial W}{\partial x}, \langle a_2 \rangle = \frac{\partial W}{\partial y}, \langle A + a_1 u + a_2 v \rangle = 0, \tag{13}$$

where

$$\langle (...) \rangle = \int \psi(...)g d\Xi.$$

Finally, the second-order time dependent gas distribution function at a cell interface is [55]

$$\begin{aligned} f(x_{p,k}, y_{p,k}, t, u, v, \xi) = &(1 - e^{-t/\tau})g_0 + ((t + \tau)e^{-t/\tau} - \tau)(\bar{a}_1 u + \bar{a}_2 v)g_0 \\ &+ (t - \tau + \tau e^{-t/\tau})\bar{A}g_0 \\ &+ e^{-t/\tau} g_r[1 - (\tau + t)(a_{1r}u + a_{2r}v) - \tau A_r)]H(u) \\ &+ e^{-t/\tau} g_l[1 - (\tau + t)(a_{1l}u + a_{2l}v) - \tau A_l)](1 - H(u)). \end{aligned} \tag{14}$$

3. Two-stage temporal discretization

The two-stage fourth-order temporal discretization which has been adopted in the previous compact fourth-order scheme on structured mesh is implemented here [24]. Following the definition of Eq. (3), a fourth-order time-accurate solution for cell-averaged conservative flow variables W_i is updated by

$$W_i^* = W_i^n + \frac{1}{2}\Delta t \mathcal{L}(W_i^n) + \frac{1}{8}\Delta t^2 \frac{\partial}{\partial t}\mathcal{L}(W_i^n), \tag{15}$$

$$W_i^{n+1} = W_i^n + \Delta t \mathcal{L}(W_i^n) + \frac{1}{6}\Delta t^2 \left(\frac{\partial}{\partial t}\mathcal{L}(W_i^n) + 2\frac{\partial}{\partial t}\mathcal{L}(W_i^*)\right), \tag{16}$$

where $\frac{\partial}{\partial t}\mathcal{L}(W)$ are the time derivatives of the summation of flux transport over closed interfaces of the cell. The proof for fourth-order accuracy can be found in [30].

For the gas-kinetic scheme, the gas evolution is a time-dependent relaxation process from kinetic to hydrodynamic scale evolution through the exponential function, and the corresponding flux becomes a complicated function of time. In order to obtain the time derivatives of the flux function at t_n and $t_* = t_n + \Delta t/2$, the flux function can be approximated as a linear function of time within a time interval. Let's first introduce the following notation,

$$\mathbb{F}_{p,k}(W^n, \delta) = \int_{t_n}^{t_n+\delta} F_{p,k}(W^n, t)\mathrm{d}t.$$

For convenience, assume $t_n = 0$, the flux in the time interval $[t_n, t_n + \Delta t]$ is expanded as the following linear form

$$F_{p,k}(W^n, t) = F_{p,k}^n + t\partial_t F_{p,k}^n.$$

The coefficients $F_{p,k}^n$ and $\partial_t F_{p,k}^n$ can be fully determined by

$$F_{p,k}(W^n, t_n)\Delta t + \frac{1}{2}\partial_t F_{p,k}(W^n, t_n)\Delta t^2 = \mathbb{F}_{p,k}(W^n, \Delta t),$$

$$\frac{1}{2}F_{p,k}(W^n, t_n)\Delta t + \frac{1}{8}\partial_t F_{p,k}(W^n, t_n)\Delta t^2 = \mathbb{F}_{p,k}(W^n, \Delta t/2).$$

By solving the linear system, we have

$$F_{p,k}(W^n, t_n) = (4\mathbb{F}_{p,k}(W^n, \Delta t/2) - \mathbb{F}_{p,k}(W^n, \Delta t))/\Delta t,$$
$$\partial_t F_{p,k}(W^n, t_n) = 4(\mathbb{F}_{p,k}(W^n, \Delta t) - 2\mathbb{F}_{p,k}(W^n, \Delta t/2))/\Delta t^2. \tag{17}$$

After determining the numerical fluxes and their time derivatives in the above equations, $\mathcal{L}(W_i^n)$ and $\frac{\partial}{\partial t}\mathcal{L}(W_i^n)$ can be obtained

$$\mathcal{L}(W_i^n) = -\frac{1}{|\Omega_i|}\sum_{p=1}^{m}\sum_{k=1}^{2}\omega_k \mathbf{F}(\mathbf{x}_{p,k}, t_n) \cdot \mathbf{n}_p, \tag{18}$$

$$\frac{\partial}{\partial t}\mathcal{L}(W_i^n) = -\frac{1}{|\Omega_i|}\sum_{p=1}^{m}\sum_{k=1}^{2}\omega_k \partial_t \mathbf{F}(\mathbf{x}_{p,k}, t_n) \cdot \mathbf{n}_p. \tag{19}$$

According to Eq. (15), W_i^* at t_* can be updated. With the similar procedure, the numerical fluxes and temporal derivatives at the intermediate stage can be constructed and $\frac{\partial}{\partial t}\mathcal{L}(W_i^*)$ is given by

$$\frac{\partial}{\partial t}\mathcal{L}(W_i^*) = -\frac{1}{|\Omega_i|}\sum_{p=1}^{m}\sum_{k=1}^{2}\omega_k \partial_t \mathbf{F}(\mathbf{x}_{p,k}, t_*) \cdot \mathbf{n}_p. \tag{20}$$

Therefore, with the solutions Eq. (18), Eq. (19), and Eq. (20), W_i^{n+1} at t_{n+1} can be updated by Eq. (16).

The traditional RK methods have well-developed stability theory and can be implemented easily. They can improve the stability for hyperbolic problems in comparison with the single stage or the Adams family of methods under the same reconstruction. The strong stability preserving (SSP) property has been analyzed for RK methods [18,17]. However, based on the time-independent flux, the Nth-order accuracy in RK methods requires no less than N stages. For a classical fourth-order RK method, four stages are needed. While for a fifth-order RK method, usually six stages are required [14]. On the other hand, the S2O4 method, which belongs to the family of MSMD method, is adopted in the current compact GKS. The MSMD methods were originally developed for numerical solutions of ODEs in the 1940s [20]. The RK methods are one subset of the MSMD methods, namely multi-stage one-derivative methods. The MSMD methods can achieve the same high-order of accuracy in time with less stages than the RK methods if the higher-order time derivatives are used. For instance, the S2O4 time marching method can get a fourth-order temporal accuracy with only two stages by adopting the flux and its first-order time derivative. The MSMD method was applied for solving PDEs very recently under DG [45] and generalized Riemann problem (GRP) [30] frameworks. Then S2O4 method was firstly applied for N-S solutions by Pan et al. [41]. There are many choices of two-stage two-derivative time integration methods, which can be used to achieve a temporal accuracy ≥ 3 [5]. Excellent work has been done for the implementation of implicit MSMD methods [23,44]. The SSP theories have been developed for two-derivative multi-stage methods recently based on different criteria [7,19]. However, since the parameters in these criteria are directly related to the time-dependent flux solvers, they haven't been validated for the compressible Euler or N-S solutions. Further studies can be conducted based on these criteria to optimize the MSMD GKS.

The use of S2O4 time integration in GKS is due to the following reasons. Firstly, the fourth-order two-derivative method with only two-stage is unique and is efficient in comparison with R-K method. Secondly, the accuracy and robustness of S2O4 time integration has been validated by numerical tests for both non-compact and compact schemes [41,26,24,40,25], and has been extended to compressible multi-component flow [37], hypersonic non-equilibrium multi-temperature flow [3], and direct simulation of compressible homogeneous turbulence [4]. The S2O4 method becomes a building block of a family of HGKS for time integration. In this work, the stability of the current scheme is tested by both smooth and discontinuous problems numerically, as shown in Subsection 5.3.

Besides the time-dependent flux function in GKS, different from the Riemann solution with a constant state at a cell interface, the gas-kinetic scheme provides a time evolution solution. Taking moments of the time-dependent distribution function in Eq. (14), the pointwise values at a cell interface can be obtained

$$W_{p,k}(t) = \int \psi f(x_{p,k}, t, u, v, \xi) d\Xi. \tag{21}$$

Similar to the two-stage temporal discretization in the flux evaluation, the time dependent gas distribution function at a cell interface is updated as

$$\begin{aligned} f^* &= f^n + \frac{1}{2}\Delta t f_t^n, \\ f^{n+1} &= f^n + \Delta t f_t^*, \end{aligned} \tag{22}$$

where a second-order evolution model is used for the update of gas distribution function on the cell interface and for the evaluation of flow variables.

In order to construct the first-order time derivative of the gas distribution function, the distribution function in Eq. (14) is approximated by the linear function

$$f(t) = f(x_{p,k}, y_{p,k}, t, u, v, \xi) = f^n + f_t^n(t - t^n).$$

According to the gas-distribution function at $t = 0$ and Δt

$$\begin{aligned} f^n &= f(0), \\ f^n + f_t^n \Delta t &= f(\Delta t), \end{aligned}$$

the coefficients f^n, f_t^n can be determined by

$$\begin{aligned} f^n &= f(0), \\ f_t^n &= (f(\Delta t) - f(0))/\Delta t. \end{aligned}$$

Thus, f^* and f^{n+1} are fully determined at the cell interface for the evaluation of macroscopic flow variables. This temporal evolution for the interface value is similar to the one used in GRP solver [11], which has a fourth-order accuracy for a compact scheme in the rectangular mesh, but may not give the same accuracy in unstructured triangular mesh. However, numerical accuracy tests demonstrate that it is enough for a third-order temporal accuracy.

The above temporal accuracy can be kept for the simulation of inviscid smooth flow. For dissipative terms, the theoretical accuracy can be only first-order in time, and the details can found in [41]. By taking benefits of the above two-stage time-stepping method, the current compact GKS with second-order flux function can achieve the expected time accuracy, which reduces the computational cost significantly in comparison with the early one-step third-order compact scheme with a third-order flux function [39].

After obtaining $W_{p,k}^{n+1}$ at each Gaussian point at cell interfaces, the cell-averaged first-order derivatives within each triangle can be evaluated

$$\bar{W}_x^{n+1} = \frac{1}{\Delta S} \oint_\Gamma W^{n+1} dy = \frac{1}{\Delta S} \sum_0^m \sum_0^2 \omega_k W_{p,k}^{n+1} \cos \alpha_p |l|_p, \tag{23}$$

$$\bar{W}_y^{n+1} = -\frac{1}{\Delta S} \oint_\Gamma W^{n+1} dx = -\frac{1}{\Delta S} \sum_0^m \sum_0^2 \omega_k W_{p,k}^{n+1} \cos \beta_p |l|_p, \tag{24}$$

where α_p is angle between the tangential direction of each edge and the positive y direction, β_p is angle between the tangential direction of each edge and the positive x direction, and $|l|_p$ is the length of each edge. The cell-averaged derivatives will be referred as cell-averaged first-order derivatives for simplicity in the following. The tangential direction is determined by "right-hand rule", a sketch is shown in Fig. 1.
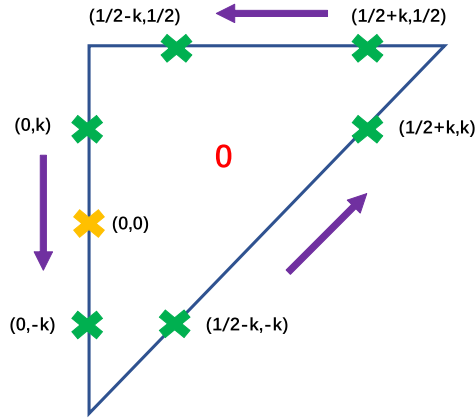
Fig. 1. Tangential direction for an isosceles right cell 0 shown by purple arrows. The length of right-angle side is 1. The locations of Gaussian points around it are labeled, where $k = \sqrt{3}/6$. (For interpretation of the colors in the figure(s), the reader is referred to the web version of this article.)

Remark 1. For a better illustration of the accuracy of cell-averaged derivatives, we evaluate the values of derivative calculated by Eq. (23) within an isosceles right cell 0 shown in Fig. 1. Assume that the fluid variable is distributed as

$$W(x, y) = a_0 + a_1 x + a_3 x^2 + a_4 y^2 + a_5 xy + a_6 x^3 + a_7 y^3 + a_8 x^2 y + a_9 xy^2. \tag{25}$$

Taking x-derivative of W, we have

$$W_x = a_1 + 2a_3 x + a_5 y + 3a_6 x^2 + 2a_8 xy + a_9 y^2. \tag{26}$$

Thus the exact averaged x-derivative over cell 0 is

$$\bar{W}_x = \frac{1}{\Delta S} \iint W_x dx dy = a_1 + \frac{2}{3} a_3 + \frac{1}{6} a_5 + \frac{1}{2} a_6 + \frac{1}{6} a_8 + \frac{1}{12} a_9. \tag{27}$$

The numerical x-derivative over cell 0 calculated by Eq. (23) is

$$\begin{aligned}
\bar{W}_x^h &= \frac{1}{2\Delta S} (W(1/2 + k, k) + W(1/2 - k, -k) - W(0, k) - W(0, -k)) \\
&= a_1 + (\frac{1}{2} + 2k^2)a_3 + 2k^2 a_5 + (\frac{1}{4} + 3k^2)a_6 + 2k^2 a_8 + k^2 a_9 \\
&= a_1 + \frac{2}{3} a_3 + \frac{1}{6} a_5 + \frac{1}{2} a_6 + \frac{1}{6} a_8 + \frac{1}{12} a_9.
\end{aligned}$$

Comparing with Eq. (27), the above numerical solution from Gaussian points around the triangle gives a fourth-order accurate representation of the cell averaged gradients. Note that the above derivatives are obtained from the time accurate evolution solution of flow variables at cell interfaces, which are different from the updated derivatives in the DG methods. Here in the compact GKS there is no direct numerical evolution equation for the cell averaged derivative.

The basic algorithm of the compact GKS is presented above. The reconstruction strategy is based on the cell averaged values and their first-order derivatives. In comparison with the popular compact DG and RDG/$P_N P_M$ methods, the similarities and differences between them are summarized as follows.

- Spatial discretization: Current compact GKS has the same reconstruction stencil as that in RDG-$P_1 P_2$ method [35]. Similar HWENO reconstructions are adopted in both methods. Thus, the current scheme has the same compactness as RDG-$P_1 P_2$ method.
- Flux solvers: DG and RDG methods are based on the weak solutions to evolve high-order moments. The corresponding volume integrals need to be evaluated. However, the cell averaged slopes in the current method are obtained by the time accurate conservative variables at the Gaussian points via the Gauss-Green theorem. Both the time accurate conservative flow variables and fluxes on the cell interface are updated from the same time-dependent gas distribution function in Eq. (14) through Eq. (21) and Eq. (5). So the volume integral is not required in the current method.
- Temporal discretization: The traditional RDG-$P_1 P_2$ uses the three-stage third-order RK method for temporal discretization [35]. The current compact GKS adopts the S2O4 time marching approach, which provides a temporal accuracy > 3 with only two stages. However, the evaluation of time-dependent gas distribution function is more expensive than that in the Riemann solver. Existing numerical results show that the computational cost of the two-stage fourth-order GKS

is similar to that of the RK4 HLLC scheme with the same WENO reconstruction and mesh number, and the GKS obtains more accurate solutions in the smooth test case [25]. The two-stage fourth-order building-block can also be adopted into the DG framework for the compressible Euler solutions with significant improvement in efficiency [6]. When solving the N-S equations, there is no additional cost in the current GKS and the final scheme has preferred accuracy, robustness, and efficiency in comparison with the Riemann solver based compact high-order schemes.

4. HWENO reconstruction

In this section, the pointwise values and the first-order derivatives of flow variables at each Gaussian point of a cell interface will be constructed. With the above initial reconstruction, the time-dependent gas distribution function at the Gaussian point can be fully determined in GKS.

4.1. Linear reconstruction

As a starting point of WENO reconstruction, a linear reconstruction will be presented first. For a piecewise smooth function $W(x, y)$ over cell Ω_i, a polynomial $P^r(x, y)$ with degrees r can be constructed to approximate $W(x, y)$ as follows

$$P^r(x, y) = W(x, y) + O(\Delta x^{r+1}, \Delta y^{r+1}).$$

In order to achieve a third-order accuracy and satisfy conservative property, the following quadratic polynomial over cell Ω_{i_0} is obtained

$$P^2(x, y) = W_{i_0} + \sum_{k=1}^{5} a_k p^k(x, y), \tag{28}$$

where W_{i_0} is the cell averaged value of $W(x, y)$ over cell Ω_{i_0} and $p^k(x, y), k = 1, ..., 5$ are basis functions, which are given by

$$\begin{cases} p^1(x, y) = x - \dfrac{1}{|\Omega_{i_0}|} \iint\limits_{\Omega_{i_0}} x dx dy, \\[2ex] p^2(x, y) = y - \dfrac{1}{|\Omega_{i_0}|} \iint\limits_{\Omega_{i_0}} y dx dy, \\[2ex] p^3(x, y) = x^2 - \dfrac{1}{|\Omega_{i_0}|} \iint\limits_{\Omega_{i_0}} x^2 dx dy, \\[2ex] p^4(x, y) = y^2 - \dfrac{1}{|\Omega_{i_0}|} \iint\limits_{\Omega_{i_0}} y^2 dx dy, \\[2ex] p^5(x, y) = xy - \dfrac{1}{|\Omega_{i_0}|} \iint\limits_{\Omega_{i_0}} xy dx dy. \end{cases} \tag{29}$$
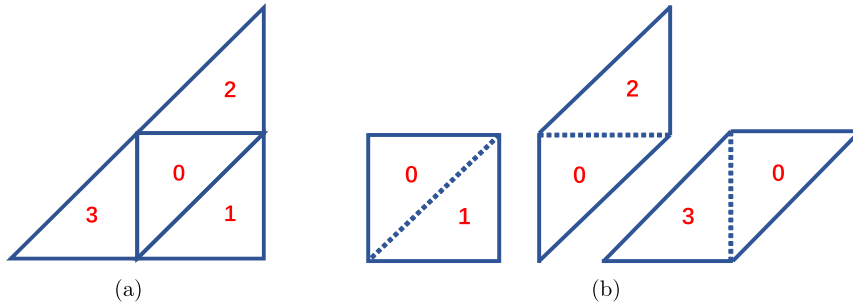
4.1.1. Large stencil and sub-stencils

In order to reconstruct the quadratic polynomial $P^2(x, y)$, the stencil for reconstruction is selected in Fig. 2, where the averages of $W(x, y)$ and averaged derivatives of $W(x, y)$ over each cell are known. For the current third-order scheme, the following values are used to obtain $P^2(x, y)$.

- Cell averages $\bar{W}$ for cell 0, 1, 2, 3
- Cell averages of the x-direction partial derivative $\bar{W}_x$ for cell "0&1", "0&2", "0&3"
- Cell averages of the y-direction partial derivative $\bar{W}_y$ for cell "0&1", "0&2", "0&3"

To determine the polynomial $P^2(x, y)$, the following conditions can be used

$$\iint\limits_{\Omega_{i_j}} P^2(x, y) dx dy = W_{i_j} |\Omega_{i_j}|,$$

$$\iint\limits_{\Omega_{i_0} + \Omega_{i_j}} \frac{\partial}{\partial x} P^2(x, y) dx dy = W_{x,i_0} |\Omega_{i_0}| + W_{x,i_j} |\Omega_{i_j}|,$$

Fig. 2. The large stencils with the inclusion of (a) cell averaged values $\bar{W}$ for cell 0, 1, 2, 3 (b) cell averaged derivatives $\bar{W}_x$ and $\bar{W}_y$ for cell "0&1", "0&2", "0&3".
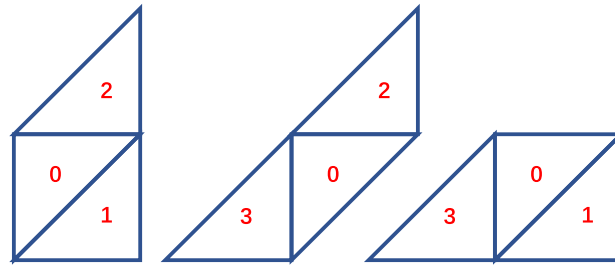
Fig. 3. The sub-stencils for compact HWENO reconstruction. From left to right, sub-stencils 1, 2, 3.

$$\iint\limits_{\Omega_{i_0}+\Omega_{i_j}} \frac{\partial}{\partial y} P^2(x, y)\mathrm{d}x\mathrm{d}y = W_{y,i_0}|\Omega_{i_0}| + W_{y,i_j}|\Omega_{i_j}|,$$

where W_{i_j} is the cell averaged value over Ω_{i_j}, W_{x,i_j} and W_{y,i_j} are the cell averaged x- and y-direction derivatives over Ω_{i_j} in a global coordinate, respectively. On a regular mesh, the system has 10 independent equations. To solve the system uniquely and avoid the singularity caused by the irregularity in the mesh, the technique in [62] has been adopted.

In order to deal with discontinuity, inspired by the existing WENO reconstruction [64], three sub-stencils $S_j, j = 1, 2, 3$ are selected from the large one given in Fig. 3. And the following cell averaged values for each sub-stencil are used to get the linear polynomial $P_j^1(x, y)$,

$$P_1^1 \text{ on } S_1 = \{\bar{W}_0, \bar{W}_1, \bar{W}_2\}, \quad P_2^1 \text{ on } S_2 = \{\bar{W}_0, \bar{W}_2, \bar{W}_3\}, \quad P_3^1 \text{ on } S_3 = \{\bar{W}_0, \bar{W}_3, \bar{W}_1\}.$$

In this reconstruction process, for a targeting cell, there is always one sub-stencil in smooth region even with the appearance of discontinuity near any one of the cell interfaces. For $j = 1, 2, 3$, the method in [62] can be used to obtain $P_j^1(x, y)$, and the linear polynomial is expressed as

$$P_j^1(x, y) = W_{i_0} + \sum_{k=1}^{2} a_{j,k} p^k(x, y). \tag{30}$$

4.1.2. Define the values of linear weights

$P^2(x, y)$ is rewritten as

$$P^2(x, y) = \gamma_0\left[\frac{1}{\gamma_0}P^2(x, y) - \sum_{j=1}^{3}\frac{\gamma_j}{\gamma_0}P_j^1(x, y)\right] + \sum_{j=1}^{3}\gamma_j P_j^1(x, y),$$

where the linear weights are chosen as $\gamma_0 = 0.97$, $\gamma_1 = \gamma_2 = \gamma_3 = 0.01$ [64] without special statement.

4.1.3. Compute the non-linear weights

The smoothness indicators $\beta_j, j = 0, 1, 2, 3$ are defined as

$$\beta_j = \sum_{|\alpha|=1}^{K} |\Omega|^{|\alpha|-1} \iint\limits_{\Omega} \left(D^\alpha P_j(x, y)\right)^2 \mathrm{d}x\mathrm{d}y,$$

where α is a multi-index and D is the derivative operator. It is proved in [64] that the smoothness indicators in Taylor series at (x_0, y_0) have the order

$$\beta_0 = O\{|\Delta_0|[1 + O(|\Delta_0|)]\} = O(|\Delta_0|),$$
$$\beta_j = O\{|\Delta_0|[1 + O(|\Delta_0|^{\frac{1}{2}})]\} = O(|\Delta_0|), j = 1, 2, 3.$$

By using a similar technique [64], we can define a global smoothness indicator σ as

$$\sigma = (|2\beta_0 - \beta_1 - \beta_2| + |2\beta_0 - \beta_2 - \beta_3| + |2\beta_0 - \beta_1 - \beta_3|)^2 = O(|\Delta_0|^3),$$

then the corresponding non-linear weights are given by

$$\delta_j = \frac{\omega_j}{\sum_{l=0}^{3} \omega_l}, \quad \omega_j = \gamma_j(1 + \frac{\sigma}{\epsilon + \beta_j}), j = 0, 1, 2, 3, \tag{31}$$

where ϵ takes 10^{-8} to avoid zero in the denominator.

The final reconstruction polynomial for the approximation of $W(x, y)$ yields

$$R(x, y) = \delta_0 [\frac{1}{\gamma_0} P^2(x, y) - \sum_{j=1}^{3} \frac{\gamma_j}{\gamma_0} P_j^1(x, y)] + \sum_{j=1}^{3} \delta_j P_j^1(x, y). \tag{32}$$

From Eq. (31), the non-linear weights approximate linear weights with $\delta_j = \gamma_j + O(|\Delta_0|^2)$, which satisfy the required accuracy condition $\delta_j = \gamma_j + O(|\Delta_0|)$ [2]. As a result, the non-linear reconstruction $R(x, y)$ achieves a third-order accuracy $R(x, y) = W(x, y) + O(|\Delta|^3)$.

4.2. Derivative reconstruction for non-equilibrium and equilibrium states

Once the conservative variables at each Gaussian points are constructed, a quadratic polynomial could be reconstructed using the cell average values W_i on cell i and all the values of the Gaussian points along the three edges of cell 0, $Q(x_{G_j}, y_{G_j}), j = 1, 2..., 6$, in a least-square sense. The derivatives of initial non-equilibrium states can be obtained by the reconstructed quadratic polynomial inside each cell. Then the equilibrium state g_0 corresponding to the conservative variables W_0 is obtained by Eq. (11). The derivatives for equilibrium state are constructed by a simple averaging of the derivatives of flow variables on both sides of the interface, which have been used in the construction of the non-equilibrium states on both sides of a cell interface.

4.3. Additional limiting technique in exceptional cases

In most cases, the above HWENO reconstruction will give physically reliable values in the determination of gas distribution functions in Eq. (14). However in extreme cases, e.g., the Mach number 20 hypersonic flow passing through a cylinder under irregular mesh, the above procedure may give unreasonable large deviations in the smooth indicators. A simple limiter is added in the above reconstruction scheme, such as

$$\text{when} \quad \beta_0 > \max(100\beta_j), \quad j = 1, 2, 3 \quad \text{then} \quad u(x, y) = W_{i_0}.$$

It will be indicated explicitly once the above limiter is used in the test cases. In fact, this criterion is so strong that it could hardly be triggered in simulation with mild discontinuities.

5. Numerical examples

In this section, numerical tests will be presented to validate the compact high-order GKS. For the inviscid flow, the collision time τ is defined by

$$\tau = \epsilon \Delta t + C|\frac{p_l - p_r}{p_l + p_r}|\Delta t,$$

where $\varepsilon = 0.01$ and $C = 1$. For the viscous flow, the collision time is related to the viscosity coefficient,

$$\tau = \frac{\mu}{p} + C|\frac{p_l - p_r}{p_l + p_r}|\Delta t,$$

where p_l and p_r denote the pressure on the left and right sides of the cell interface, μ is the dynamic viscous coefficient, and p is the pressure at the cell interface. In smooth flow region, it reduces to $\tau = \mu/p$. The ratio of specific heats takes $\gamma = 1.4$. The reason for including pressure jump term in the particle collision time is to add artificial dissipation in the discontinuous region, where the numerical cell size is not enough to resolve the shock structure, and the enlargement of

collision time is to keep the non-equilibrium in the kinetic flux function to mimic the real physical mechanism in the shock layer.

Same as many other high-order schemes, all reconstructions will be done on the characteristic variables. Denote $F(W) = (\rho U, \rho U^2 + p, \rho UV, U(\rho E + p))$ in the local coordinate. The Jacobian matrix $\partial F / \partial W$ can be diagonalized by the right eigenmatrix R. For a specific cell interface, R_* is the right eigenmatrix of $\partial F / \partial W^*$, and W^* are the Roe-averaged conservative flow variables from both sided of the cell interface. The characteristic variables for reconstruction are defined as $U = R_*^{-1} W$.

Second-order boundary conditions are mainly adopted in the current scheme. For each boundary cell, one ghost cell is constructed according to the corresponding boundary condition. Then a linear least-square for smooth flow or min-mod reconstruction for discontinuous flow is adopted for the boundary cell reconstruction. After we obtain the inner state at the boundary, a ghost state can be assigned according to boundary condition, and the corresponding gas distribution function in Eq. (14) can be determined. A high-order curved boundary reconstruction is only applied to the test of subsonic flow passing through a circular cylinder. Further explorations are still needed on constructing a stable compact high-order reconstruction on curved boundaries.

The time step is determined by

$$\Delta t = C_{CFL} \mathrm{Min}(\frac{\Delta r_i}{||\mathbf{U}_i|| + (a_s)_i}, \frac{(\Delta r_i)^2}{4\nu_i}), \tag{33}$$

where C_{CFL} is the CFL number, and $||\mathbf{U}_i||$, $(a_s)_i$, and $\nu_i = (\mu/\rho)_i$ are the magnitude of velocities, sound speed, and kinematic viscosity coefficient for cell i. The Δr_i takes the same value as in the RK-DG method [8], which is the radius of the inscribed circle in that cell. Generally, the CFL number could safely take a value around 0.5 in the cases without extremely strong shocks or highly irregular mesh.

5.1. Accuracy test

(a) 2-D sinusoidal wave propagation

The advection of density perturbation is commonly used to test the order of accuracy of a numerical scheme for the smooth Euler solution. The initial condition is given as a sinusoidal wave propagating in the diagonal direction

$$\rho(x, y) = 1 + 0.2 \sin(\pi (x + y)),$$
$$U(x, y) = 1, V(x, y) = 1, p(x, y) = 1,$$

with the exact solution

$$\rho(x, y, t) = 1 + 0.2 \sin(\pi (x + y - 2t)),$$
$$U(x, y, t) = 1, V(x, y, t) = 1, p(x, y, t) = 1.$$

For the current compact reconstruction, we also need the derivative information. For this sin-wave test case, the initial derivative distributions of primary variables are given by

$$\partial_x \rho(x, y) = \partial_y \rho(x, y) = 0.2\pi \cos(\pi (x + y)),$$
$$\partial_x U(x, y) = \partial_y U(x, y) = 0,$$
$$\partial_x V(x, y) = \partial_y V(x, y) = 0,$$
$$\partial_x P(x, y) = \partial_y p(x, y) = 0,$$

and the initial derivatives of conservative variables can be calculated by the chain rule.

The computational domain is $[0, 2] \times [0, 2]$ and $N \times N \times 2$ uniform triangular meshes are used with periodic boundary condition in both directions. The time step is determined by $CFL = 0.5$. First the linear weights are chosen as $\gamma_0 = 1.0$, $\gamma_j = 0.0$, $j = 1, 2, 3$, where a smooth polynomial will be constructed solely on the large stencil in a least-squares sense. The L^1, L^2 and L^∞ errors and convergence orders are presented in Table 1. The expected third-order of accuracy is obtained. Next the linear weights are chosen as $\gamma_0 = 0.97$, $\gamma_j = 0.01$, $j = 1, 2, 3$. In this case, the non-linear weights will take effects on coarse mesh due to the discontinuities. For instance, the absolute errors obtained by non-linear weights in Table 2 with mesh number $10 \times 10 \times 2$ is about two times larger than those obtained by linear weights in Table 1. With a continuous mesh refinement, the convergence order tends to be uniform and the absolute error gets close to the one shown in Table 1. This demonstrates that the current reconstruction strategy with non-linear weights could keep third-order accuracy even with possible existing extrema [2], which is consistent with the proof in [64].

(b) Subsonic flow past a circular cylinder

This test has been widely used to test the spatial accuracy for a high-order scheme with curved wall boundary [28,34,49]. A circular cylinder is put in the center of the computational domain with a radius of $r_0 = 0.5$. The concentric computational

Table 1
Accuracy test for the 2-D sin-wave propagation: the linear weights are chosen as $\gamma_0 = 1.0$, $\gamma_j = 0.0$, $j = 1, 2, 3$.

Mesh number	L^1 error	Order	L^2 error	Order	L^∞ error	Order
$5 \times 5 \times 2$	1.09599e-1		1.22089e-1		1.69340e-1	
$10 \times 10 \times 2$	7.02772e-3	3.96	7.98434e-3	3.94	1.08584e-2	3.96
$20 \times 20 \times 2$	4.97718e-4	3.82	5.53952e-4	3.85	7.82567e-4	3.79
$40 \times 40 \times 2$	4.28788e-5	3.54	4.76667e-5	3.54	6.74011e-5	3.54

Table 2
Accuracy test for the 2-D sin-wave propagation: the linear weights are chosen as $\gamma_0 = 0.97$, $\gamma_j = 0.01$, $j = 1, 2, 3$.

Mesh number	L^1 error	Order	L^2 error	Order	L^∞ error	Order
$5 \times 5 \times 2$	1.20657e-1		1.36454e-1		2.10342e-1	
$10 \times 10 \times 2$	1.19812e-2	3.33	1.36311e-2	3.32	2.12012e-2	3.31
$20 \times 20 \times 2$	1.08292e-3	3.47	1.46125e-3	3.22	3.03906e-3	2.80
$40 \times 40 \times 2$	4.48604e-05	4.59	5.2003e-05	4.81	9.5303e-05	4.99
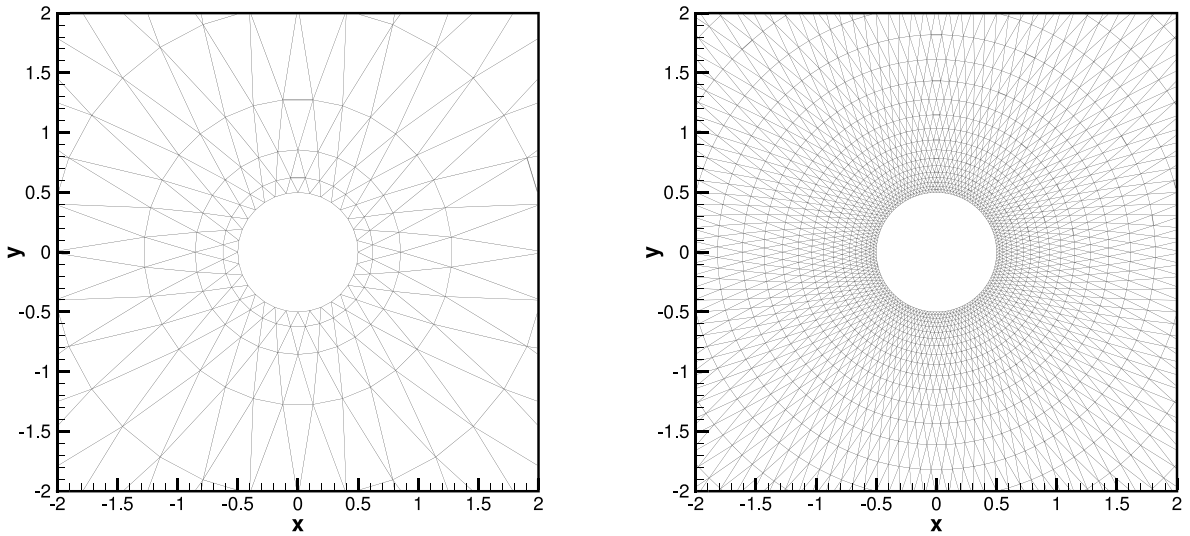
Fig. 4. The mesh samples for the subsonic inviscid flow passing through a circular cylinder. Left: $16 \times 4 \times 2$ cells. Right: $64 \times 16 \times 2$ cells.

domain is bounded by a circle $r_{out} = 20$. Four successively refined meshes with $16 \times 4 \times 2$, $32 \times 8 \times 2$, $64 \times 16 \times 2$, and $128 \times 32 \times 2$ cells are given according to [28]. Mesh distributions are shown in Fig. 4. The reflective boundary condition is imposed on the wall of cylinder. The far-field boundary condition is set around the outside of the domain, which has a free stream condition

$$(\rho, U, V, p)_\infty = (1, 0.38, 0, \frac{1}{\gamma}),$$

where $\gamma = 1.4$. It describes a subsonic inviscid flow at $Ma_\infty = 0.38$ passing through a cylinder. Ideally, the flow is isentropic with

$$S(x, y, t) = S_\infty.$$

Thus, an entropy error, defined as

$$\epsilon_s = \frac{S - S_\infty}{S_\infty} = \frac{p}{p_\infty}(\frac{\rho_\infty}{\rho})^\gamma - 1,$$

is used for measuring the error of the numerical solution. The simulation is initialized with the free stream value. The L^2-error is recorded when the flow gets to a steady state. To achieve a third-order accuracy on the cylinder wall, a one-side compact stencil with three cells 0, 1, 2 is used to reconstruct a smooth polynomial within a boundary cell 0. A quadratic polynomial within a boundary cell is determined in a least-squares sense and this stencil includes nine data, i.e.,

- cell averages $\bar{W}$ for cell 0, 1, 2,
- cell averages of the x-direction partial derivative $\bar{W}_x$ for cell 0, cell 1, cell 2,

Table 3
Accuracy test for the subsonic inviscid flow passing through a circular cylinder. Both straight and curved boundary treatments are applied with a third-order compact boundary reconstruction.

Mesh number	Straight B.C.		Curved B.C.	
	L^2 error	order	L^2 error	order
$16 \times 4 \times 2$	2.03e-3		1.86e-03	
$32 \times 8 \times 2$	2.27e-04	3.16	1.68e-4	3.47
$64 \times 16 \times 2$	5.35e-05	2.09	2.24e-5	2.91
$128 \times 32 \times 2$	1.38e-05	1.95	2.24e-6	3.32
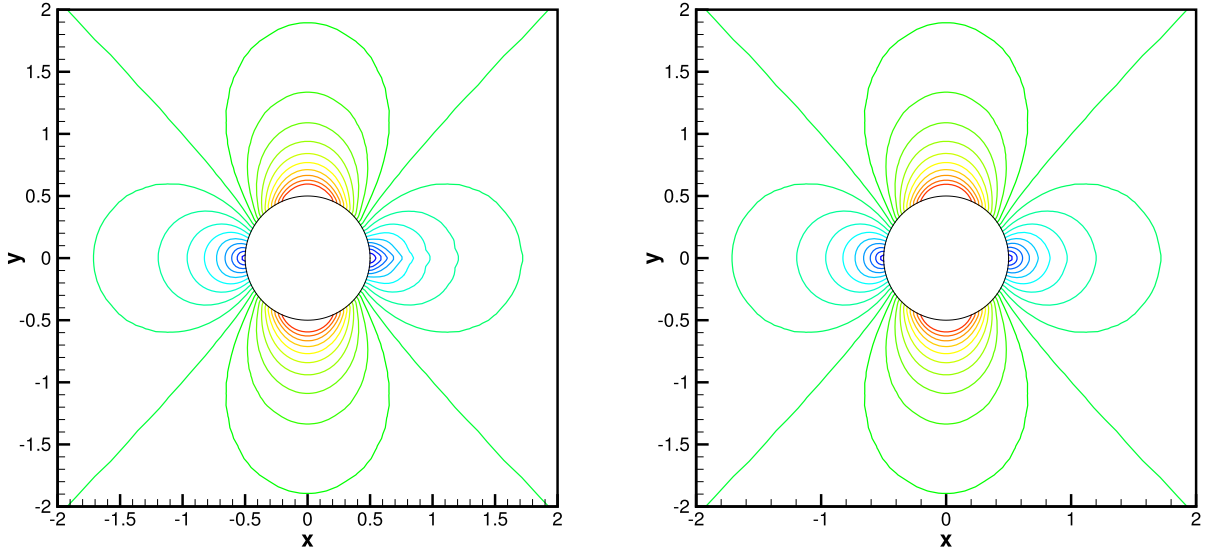
Fig. 5. Subsonic flow passing through a circular cylinder: 20 equidistant Mach contours from 0.038 to 0.76. Mesh $128 \times 32 \times 2$. Left: straight boundary approximation. Right: curved boundary treatment.

- cell averages of the y-direction partial derivative $\bar{W}_y$ for cell 0, cell 1, cell 2.

To study the effect from the curved boundary treatment, both straight boundary approximation and curved boundary treatment with the modification of the normal directions of the boundary Gaussian points, as proposed in [28], are tested. The results obtained by the current compact GKS are shown in Table 3. Only the compact GKS with the curved boundary treatment can achieve a third-order spatial accuracy, which is consistent with the results in [28,34,49]. The numerical result with straight boundary approximation has a more visible wake than that with curved boundary treatment, as shown in Fig. 5.

5.2. Mesh adaptability

One-dimensional Riemann problems are well-designed and commonly-used to test the performance of a numerical scheme for compressible flow. It is important to test the current scheme under irregular unstructured mesh in these problems. Several test cases will be used to evaluate the mesh adaptability, stability and computational efficiency of the current method.

Remark 2. Three types of mesh are used to test the mesh adaptability in this paper, which is shown on the left side of Fig. 6. The first type contains only isosceles right triangles, referred as uniform mesh. The second type is generated through the "Frontal" algorithm, and the third one through the "Delaunay" algorithm by using the Gmsh [15]. They are referred as regular and irregular meshes respectively.

(a) Sod problem
The initial condition for the Sod test case is given as follows

$$(\rho, U, p) = \begin{cases} (1, 0, 1), 0 \leq x < 0.5, \\ (0.125, 0, 0.1), 0.5 \leq x \leq 1. \end{cases}$$
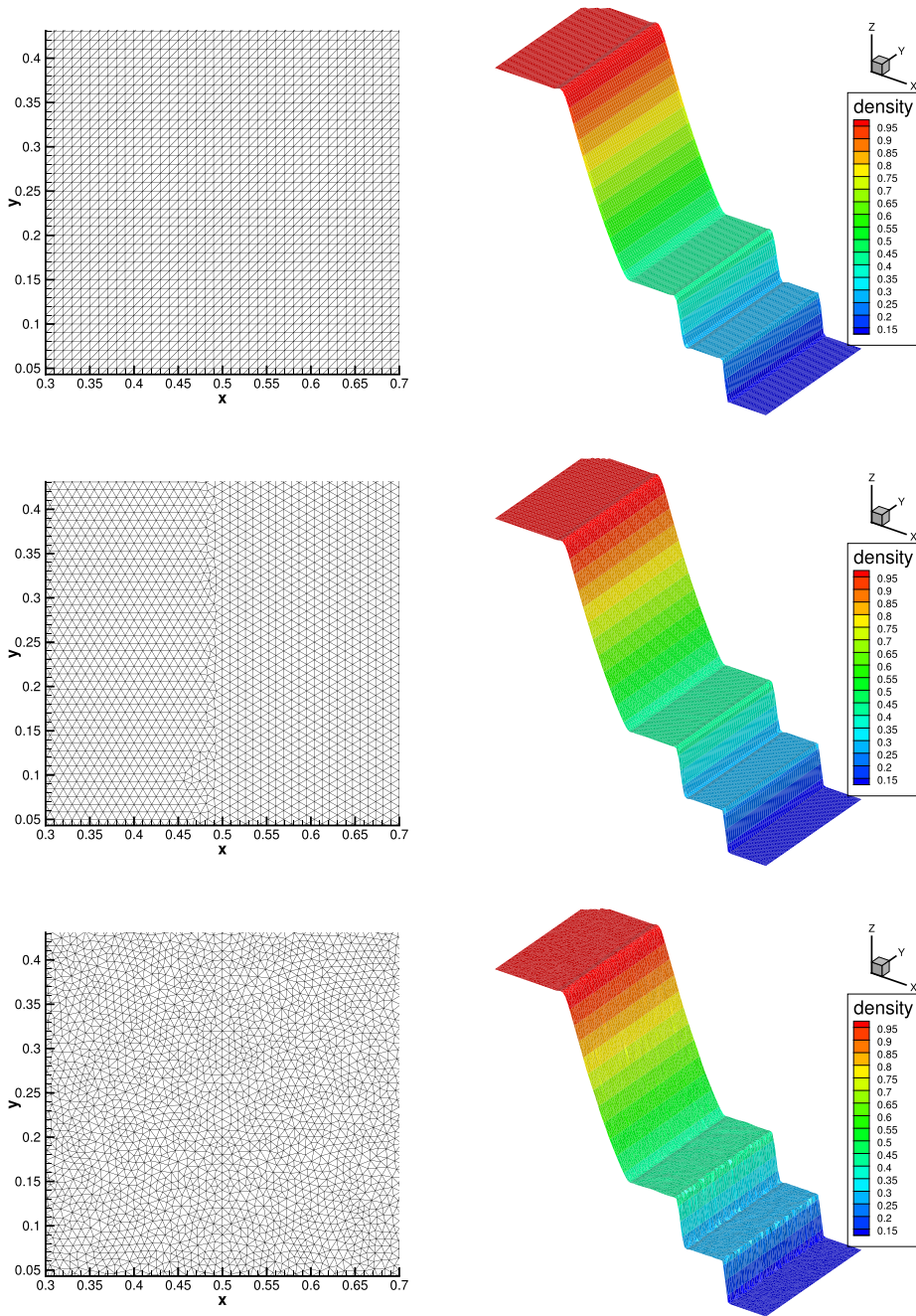
Fig. 6. Sod problem: the meshes and 3-D view of density distributions at $t = 0.2$ with cell size $1/100$. The meshes are referred as uniform mesh, regular mesh, and irregular mesh from the top to bottom.

The computational domain is $[0, 1] \times [0, 0.5]$, and the mesh size is $h = 1/100$. Non-reflection boundary condition is adopted at the left and right boundaries of the computational domain, and periodic boundary condition is adopted at the bottom and top boundaries of the computational domain. The computations are performed under uniform, regular, and irregular meshes. The 3-D plot of density distributions in Fig. 6 shows the uniformity in the flow distributions along y direction even with irregular mesh. The density, velocity, and pressure distributions at the center horizontal line on different meshes are also extracted, as shown in Fig. 7. To evaluate the mesh dependence of the proposed scheme quantitatively, the absolute errors of the extracted line data against the exact Riemann solution are listed in Table 4. Since the error near the discontinuity is much larger than these in smooth region, the L^{∞} error is much larger than the others. The scheme shows good mesh tolerance with relative L^{∞} error $\leq 3\%$ among different meshes.
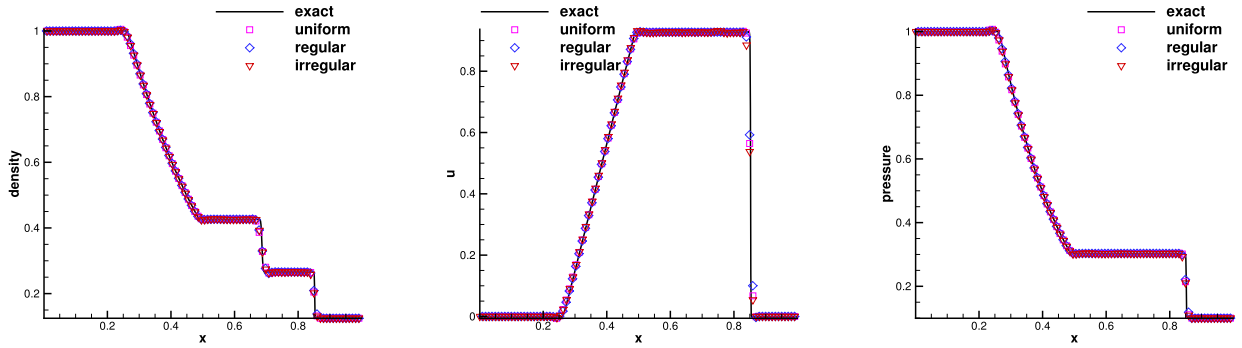
Fig. 7. Sod problem: density, velocity, and pressure distributions at $t = 0.2$ with cell size $1/100$ along the center horizontal lines under different meshes.

Table 4
Sod problem: density error under different meshes with cell size $h = 1/100$. 101 point-wise data are extracted along the center horizontal line.

Mesh type	L^1 error	L^2 error	L^∞ error
Uniform	2.926e-3	9.792e-3	6.385e-2
Regular	2.625e-3	9.419e-3	6.343e-2
Irregular	2.792e-3	9.632e-3	6.511e-2

Table 5
Shu-Osher problem: density error under different meshes with cell size $h = 1/40$. 401 point-wise data are extracted along the center horizontal line.

Mesh type	L^1 error	L^2 error	L^∞ error
Uniform	2.457e-2	6.806e-2	1.074e0
Regular	2.561e-2	6.916e-2	1.076e0
Irregular	2.945e-2	7.404e-2	1.050e0

(a) Shu-Osher problem

To test the performance of capturing high frequency wave, the Shu-Osher problem [46] is tested, which is a case with the density-shock wave interaction. The initial condition is given as follows

$$(\rho, U, p) = \begin{cases} (3.857134, 2.629369, 10.33333), & 0 \le x \le 1, \\ (1 + 0.2\sin(5x), 0, 1), & 1 < x \le 10. \end{cases}$$

The computational domain is $[0, 10] \times [0, 0.25]$ and the triangular mesh with $h = 1/40$ is used. The periodic boundary condition is applied in the y-direction. Numerical results under different meshes are presented in Fig. 8. The extracted density profiles with 401 points along the horizontal line are plotted. The reference solution is obtained by the 1-D fifth-order WENO GKS [26] with 10, 001 interfaces. The current third-order results are even compatible with the traditional S2O4 GKS with WENO5-Z reconstruction [41]. For the same mesh size, due to more cells used in the non-uniform mesh case than the uniform one, the results from regular and irregular meshes capture extremes slightly better than the case of uniform one. The 3-D density distributions are presented in Fig. 9. The numerical results preserve the uniformity along y-direction nicely even with the existence of acoustic waves in a large scale. The errors for the compact scheme with different meshes are given in Table 5. The L^∞ errors are very close to each other, which again demonstrates good mesh adaptability of the current scheme. The L^1 errors are on the order of 10^{-2}. The current scheme can resolve the acoustic wave accurately.

5.3. Stability test

There are well-defined stability theories for the popular DG methods [10]. For the Mth-order RDG/$P_N P_M$ ($M \ge N$), it has been proved in 1-D case the CFL is restricted as the same Nth-order DG method [13]. For the traditional high-order finite volume method, the von Neumann stability analysis can be directly conducted with a set of specified reconstruction, flux solver, and time-stepping method under the linear smooth case [50,48]. Such analysis is convenient under 1-D structured mesh. However, so far we don't have the ability to give a theoretical analysis of the stability property of the current scheme for even the linear case based on triangular mesh. The stability of the current scheme is studied numerically by changing the CFL number in the test cases. Uniform mesh is used to exclude the influence of mesh topology. The sinusoidal wave propagation is used for the linear stability test with linear reconstruction. As shown in Fig. 10(a), the expected convergence orders (≥ 3) are obtained from different CFL numbers from 0.1 to 1.7. As the CFL number increases, the L^1 error increases and the convergence order approaches to 3. Then the Sod problem is used to test the non-linear stability with non-linear
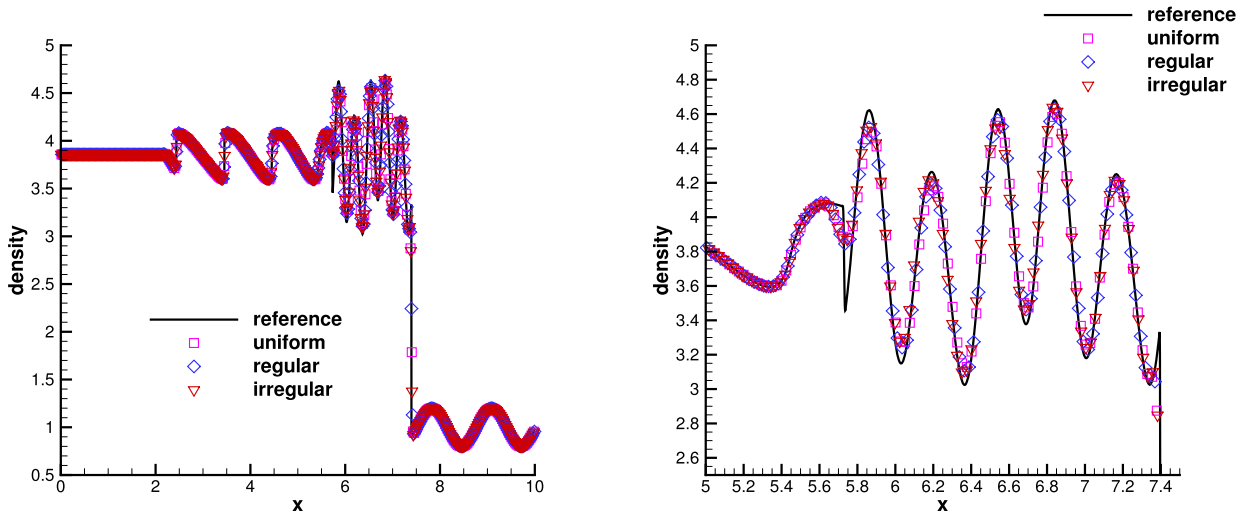
Fig. 8. Shu-Osher problem: the density distributions and local enlargement at $t = 1.8$ with cell size 1/40 along the center horizontal line under different meshes.
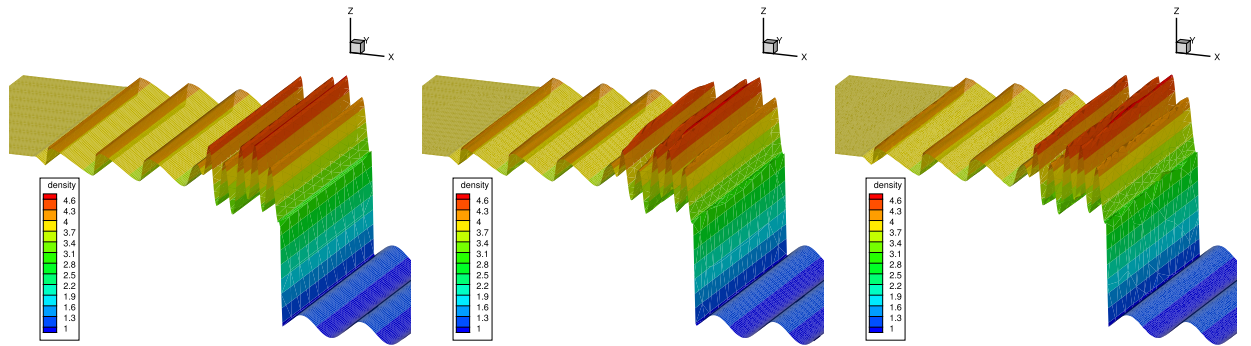

Fig. 9. Shu-Osher problem: the 3-D view of density distributions at $t = 1.8$ with cell size 1/40 under different meshes. From left to right: uniform mesh, regular mesh, and irregular mesh.

reconstruction. The numerical solutions are essentially non-oscillatory with a CFL number (≤ 1.3), as shown in Fig. 10(b). As the linear stability limit is approached, the result becomes oscillatory. More theoretical study can be done in the future. The limit of CFL number seems larger than that for the non-compact two-stage fourth-order WENO5-GKS [41], which may be due to the different definition of cell characteristic length Δr_i in Eq. (33). Through the above tests, we show that the scheme is basically stable under the conventional CFL condition. The wave profiles can be well resolved with a CFL number around 0.5.

5.4. Computational efficiency

Based on the above Sod test case, the computational efficiency from the current method will be evaluated. To make an assessment of the efficiency of the current scheme, the comparisons with other schemes are conducted. The CPU times are recorded after running 10 explicit time steps for each scheme with a single processor of Intel Xeon E5 2630v4 @2.10 GHz in both cases.

First, the current method is compared with two different two-stage schemes: the original S2O4 GKS based on non-compact WENO5-Z reconstruction [41] and the compact S2O4 GKS based on HWENO reconstruction [24]. Characteristic variables are used for reconstruction in all three schemes and two Gaussian points are used at each cell interface. With the same number of cells, the new method is slightly slower than other two schemes, as shown in Table 6.

Next, the schemes with different reconstruction methods and different time marching approaches are compared. These methods are developed from the same in-house GKS codes. The computational time is shown in Table 7. The second-order GKS on triangular mesh uses a min-mod limiter reconstruction, which is the same as that in [39]. From the simulation results, the new compact-GKS is about 5 times slower than the typical second-order GKS (case I) and only about 30% slower than the second-order GKS (case II) when the same time discretization and Gaussian points are used. The high efficiency of reconstruction used in the current scheme is mainly due to three reasons. Firstly, the coefficients for linear

(a)   (b)
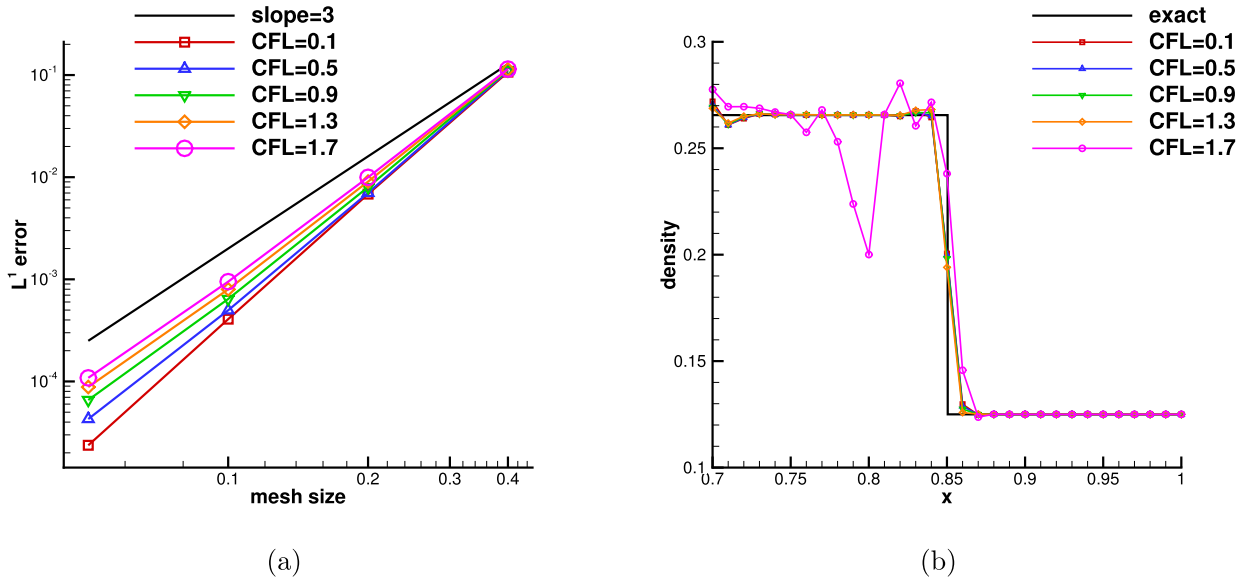
Fig. 10. Stability test under different CFL numbers. (a) L^1 errors for sinusoidal wave propagation. (b) The local enlargement of density distributions for Sod problem.

Table 6
Computational time (in seconds) of different schemes for the 1D Sod problem. The results are obtained after 10 explicit time steps by an in-house C++ code with a single core of Intel Xeon 2630v4 @ 2.10 GHz. Characteristic reconstruction is used for all three schemes.

Scheme	No. of cell	No. of interface	CPU time
Structured S2O4-WENO-GKS [41]	10000	20200	3.51s
Structured compact S2O4-HWENO-GKS [24]	10000	20200	4.00s
Triangular compact-GKS	10000	15150	4.80s

Table 7
Computational time (in seconds) of different schemes for the 1-D Sod problem. The results are obtained after 10 explicit time steps by an in-house C++ code with a single core of Intel Xeon 2630v4 @ 2.10 GHz. The same uniform triangular mesh with 10000 cells and 15150 interfaces are used for all three schemes.

Scheme	No. of stage	No. of Gauss point	CPU time
Triangular second-order GKS Case I	1	1	0.81s
Triangular second-order GKS Case II	2	2	3.68s
Triangular compact-GKS	2	2	4.80s

reconstruction could be all pre-stored in memory. Secondly, the linear weights are arbitrarily chosen and independent from geometry [64]. Thirdly, all the reconstruction procedure could be performed under a global coordinate.

5.5. Woodward-Colella blast wave

The Woodward-Colella blast wave problem [53] is considered, and the initial condition is given as follows

$$(\rho, U, p) = \begin{cases} (1, 0, 1000), & 0 \leq x < 10, \\ (1, 0, 0.01), & 10 \leq x < 90, \\ (1, 0, 100), & 90 \leq x \leq 100. \end{cases}$$

The computational domain is $[0, 100] \times [0, 2.5]$ and a uniform mesh with $400 \times 10 \times 2$ is used. The periodic boundary condition is applied in the y direction. The extracted density profiles with 401 points along the horizontal line from the current compact GKS and second-order GKS at $t = 3.8$ are shown in Fig. 11. The reference solution is obtained by the 1-D fifth-order WENO GKS [26] with 10,001 interfaces. It shows that the current compact scheme can resolve the wave profiles clearly better than the non-compact third-order scheme [64], particularly for the local extreme values. The left contact discontinuity behaves relatively diffusive. Moreover, the uniformity in the flow distribution along y direction is well kept in the strong shock case, see Fig. 11. The quantitative value of the error relative to the reference solution is given in Table 8. For
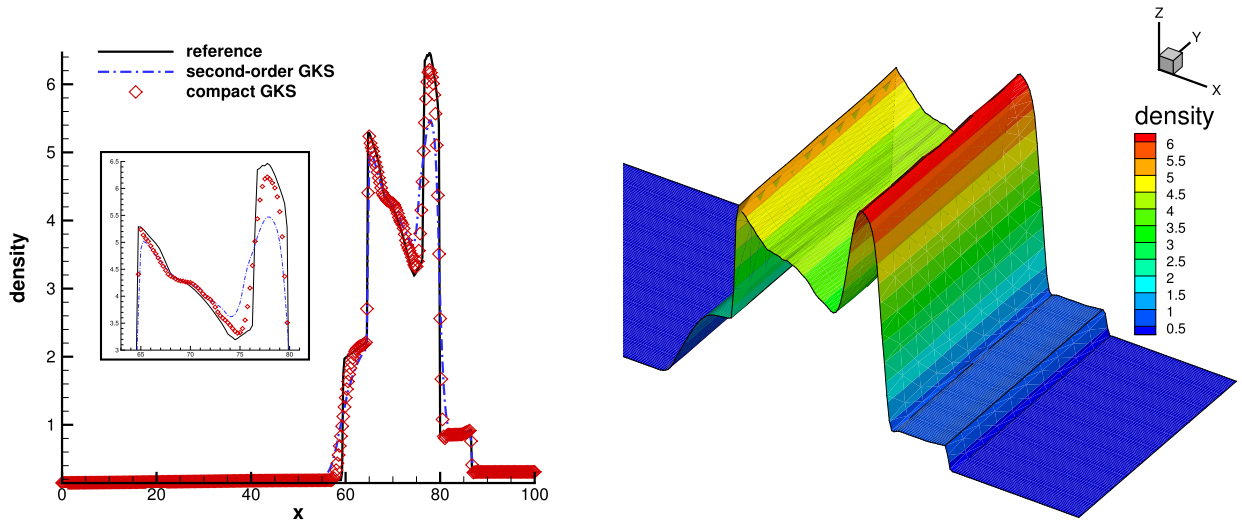
Fig. 11. Woodward-Colella blast wave problem: the density distribution along the center horizontal line and its 3-D view under a uniform mesh at $t = 3.8$ with cell size $h = 1/4$. CFL $= 0.4$.

Table 8
Woodward-Colella blast wave problem: density error of different schemes under a uniform mesh with cell size $h = 1/4$. 401 point-wise data are extracted along the center horizontal line.

Scheme	L^1 error	L^2 error	L^∞ error
Second-order GKS	1.245e-1	3.302e-1	1.994e0
Compact GKS	6.502e-2	2.117e-1	1.765e0

Table 9
Noh problem: density errors of different schemes under a regular mesh with cell size $h = 1/4$. 401 point-wise data are extracted along the center horizontal line.

Scheme	L^1 error	L^2 error	L^∞ error
Second-order GKS	2.960e-2	1.453e-1	2.165e0
Compact GKS	1.955e-2	1.566e-1	2.754e0

the current case, the error of the compact GKS and the second-order one has no significant difference. The strong numerical shock may contribute mainly to the overall error of the scheme.

5.6. Noh problem

The one dimensional Noh problem [32] is considered. The initial condition is given as

$$(\rho, U, p) = \begin{cases} (1, 1, 10^{-6}), & 0 \le x < 50, \\ (1, -1, 10^{-6}), & 50 \le x \le 100, \end{cases}$$

with $\gamma = 1.4$ in the current test. The computational domain is $[0, 100] \times [0, 2.5]$ and a regular mesh with $400 \times 10 \times 2$ is used. The periodic boundary condition is applied in the y direction. The initial setting generates two infinite strength shocks moving towards both sides of the boundaries. The state behind the shocks has a huge jump on pressure. The limiting technique is required for this case. The extracted density profile with 401 points along the horizontal line obtained by both the compact GKS and second-order GKS at $t = 50$ are shown in Fig. 12. It can be observed that the symmetry is broken obviously and quite badly. The possible reason is that the limiter is triggered around the strong shock and consequently introduces large reconstruction error on the non-uniform mesh. The compact scheme has less oscillation in the central high-density region than the second-order scheme and captures the shock sharply with less cells. The quantitative error of the compact scheme against the exact solution is also given in Table 9. The L^∞ error is influenced largely by the strong numerical shock.
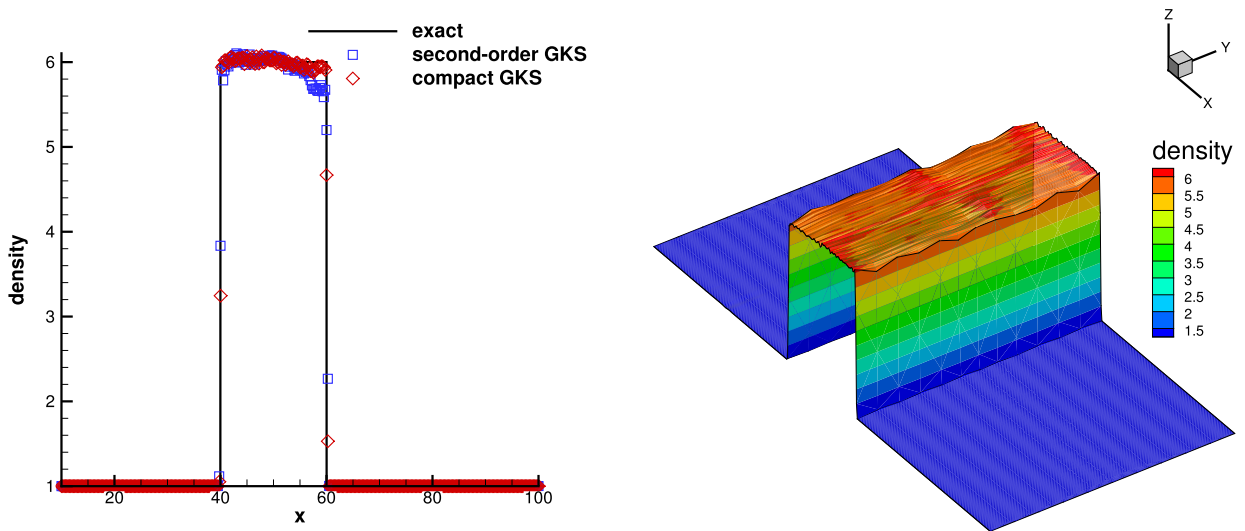
Fig. 12. Noh problem: the density distribution along the center horizontal line and its 3-D view under a regular mesh at $t = 50$ with cell size $h = 1/4$.

Table 10
123 problem: internal energy error of different schemes under a regular mesh with cell size $h = 1/4$. 401 point-wise data are extracted along the center horizontal line.

Scheme	L^1 error	L^2 error	L^∞ error
Second-order GKS	2.792e-2	8.227e-2	5.720e-1
Compact GKS	1.622e-2	6.014e-2	5.498e-1

5.7. 123 problem

The 123 problem [32] is tested with the initial condition

$$(\rho, U, p) = \begin{cases} (1, -2, 0.4), & 0 \leq x < 50, \\ (1, 2, 0.4), & 50 \leq x \leq 100. \end{cases}$$

The solution yields two strong rarefaction waves and leaves a near-vacuum state in the center with both density and pressure close to zero, as shown in Fig. 13. The limiting technique in subsection 4.3 is required for this case. The mesh and boundary conditions are the same as those in the Noh problem. High-order schemes can get failed easily in this case with negative internal energy. While both compact and traditional low-order GKS give a spurious peak in the internal energy, which is similar to other Eulerian methods [32]. The result by the compact scheme is closer to the exact solution than the low-order one, as shown in Fig. 13(d). Considering the high contrast in the density distributions, the internal energy errors are dominant instead, as shown in Table 10.

5.8. High-contrast shock tube

High-contrast shock tube problems are widely tested by the Lagrangian method [33] and the positive preserving limiters for high-order method [22]. Remarkable solutions have been obtained by the high-order GRP solvers [30,11]. Here the initial setting follows [47] as

$$(\rho, U, p) = \begin{cases} (10^N, 0, 10^N), & 0 \leq x < 30, \\ (1, 0, 1), & 30 \leq x \leq 100, \end{cases}$$

where a pressure ratio 10^N, $N = 1, 2, 3...$ is used. The mesh and boundary conditions are the same as those in the Noh problem. The current scheme can survive for N up to 5 with the implementation of limiter in subsection 4.3. The numerical results with $N = 5$ are shown in Fig. 14. The initial high pressure ratio generates a very strong rarefaction wave, which leads to a large deviation of the locations of the numerical shock and contact discontinuity from the exact ones. It can be observed from the density and pressure distributions that the shock location can be improved with mesh refinement, while the contact discontinuity has marginal improvement. The Lagrangian method [33] and the GRP scheme [30] perform nicely
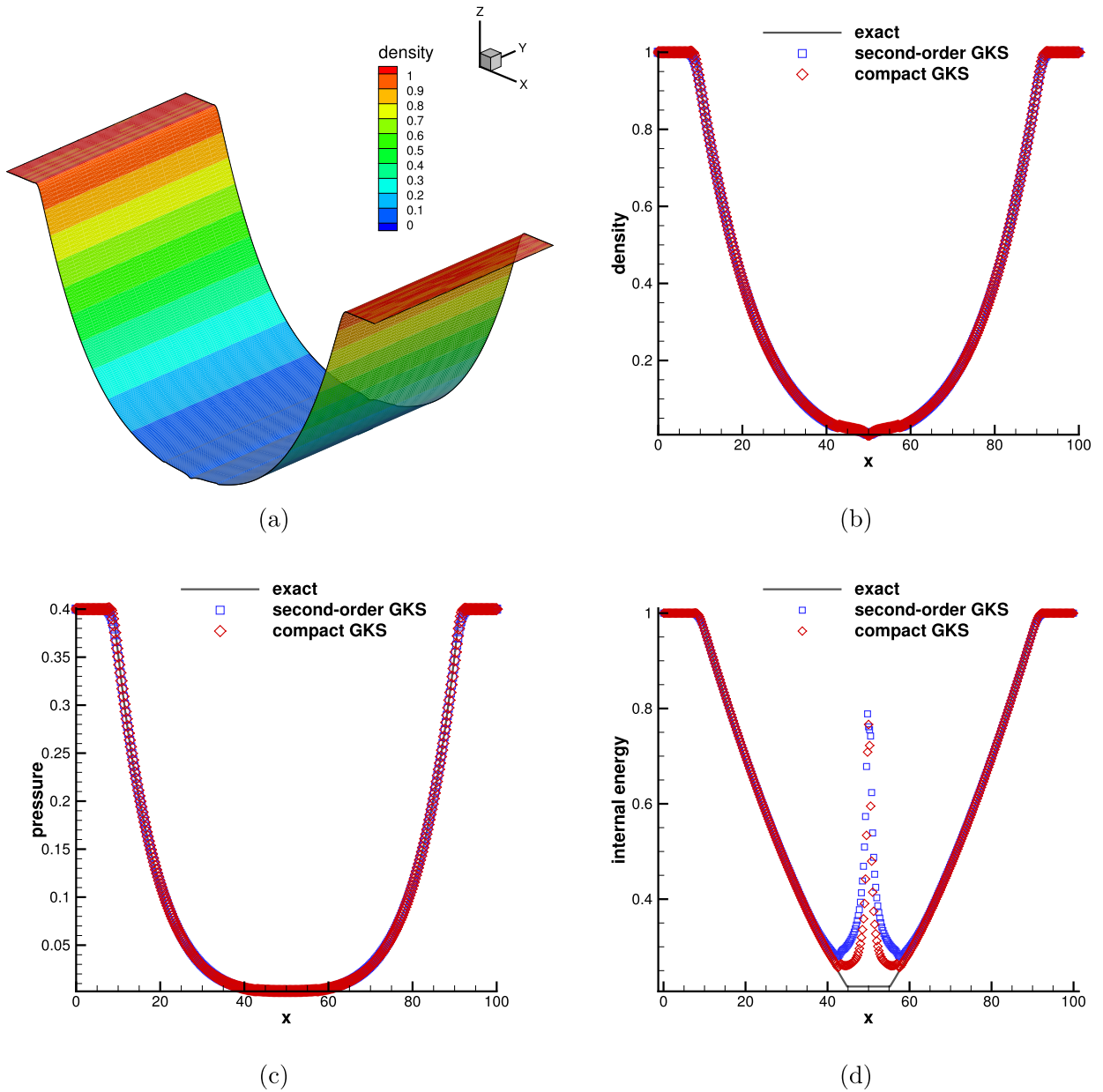
Fig. 13. 123 problem under a regular mesh at $t = 15$ with cell size $h = 1/4$. (a) The 3-D view of density distribution. (b)-(d) The density, pressure, and internal energy distributions for different schemes along the center horizontal line.

in this case due to the use of the exact Riemann solution, especially in the initial a few time steps. As shown in Fig. 15, the uniformity of flow field along y-direction is well kept by the compact scheme. The log scale density profiles show that the third-order compact GKS gives more accurate solution than the second-order one. The internal energy error from these two schemes is presented in Table 11. The differences in Fig. 15 between the GKS and Riemann solutions are mainly from their different physical modeling at the initial few time steps. With such a huge density and pressure jump as the initial condition, due to the enlarged particle collision time the GKS will use the kinetic scale particle free transport in the flux evaluation which cannot identify the Riemann solution of the Euler equations. The error from the initial few time steps is kept by GKS in the following computation. If the initial condition for this test case is based on the exact Euler solution at time $t > 0$, such as using the resolved exact Riemann solution by a few cells as the initial condition, the final numerical solution from the GKS can be much improved [38].
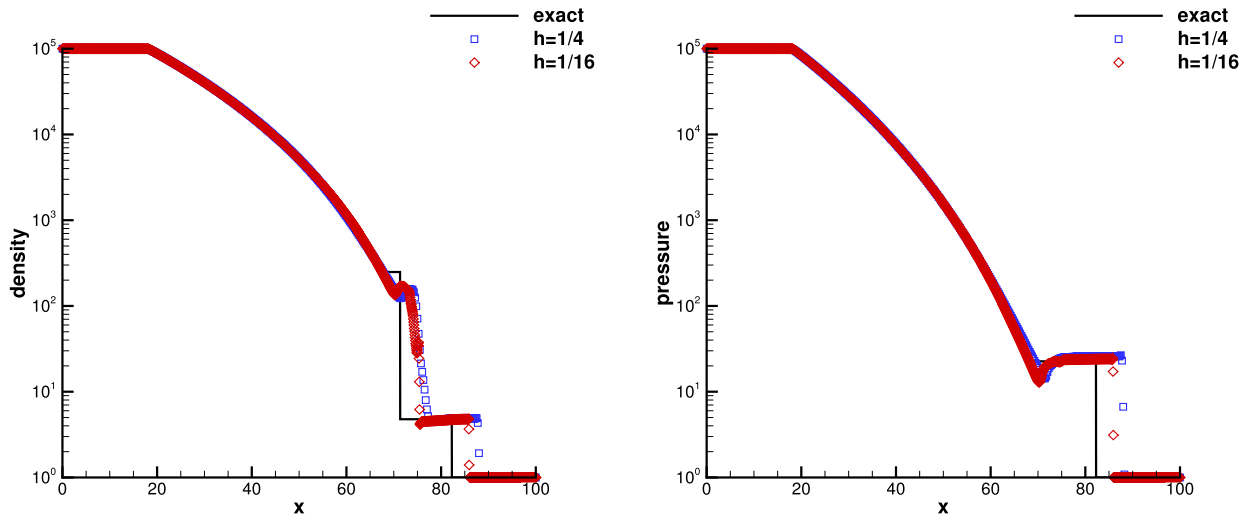
Fig. 14. High-contrast shock tube: the density and pressure distributions along the center horizontal line at $t = 10$ with different cell sizes by the compact GKS.
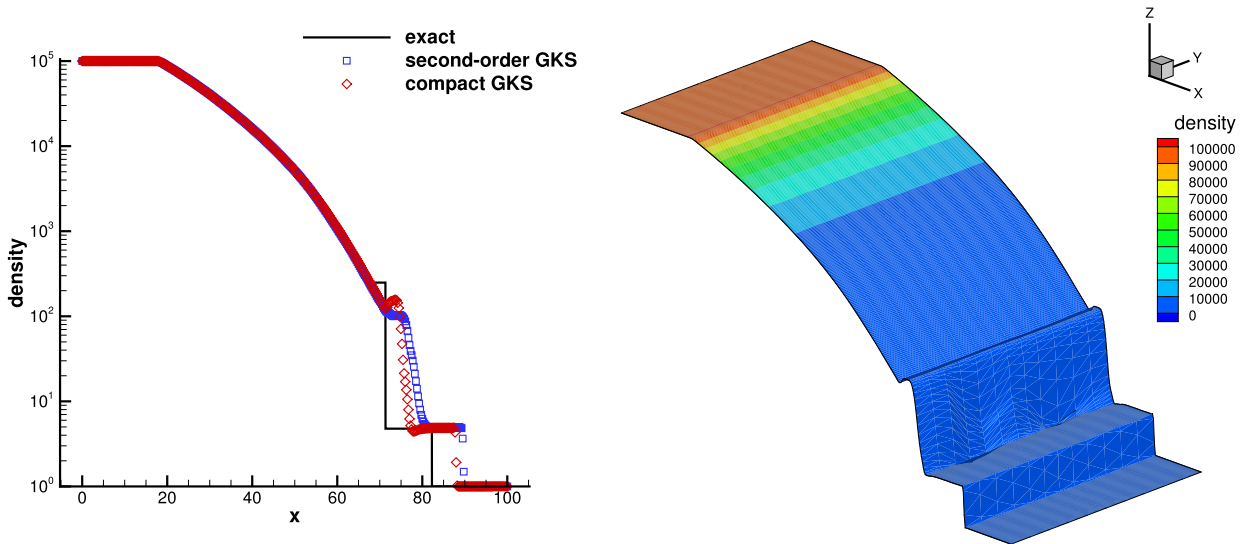
Fig. 15. High-contrast shock tube: the density distribution along the center horizontal line and its 3-D view under a regular mesh at $t = 10$ with cell size $h = 1/4$.

Table 11
High-contrast shock tube: internal energy error of different schemes under a regular mesh with cell size $h = 1/4$. 401 point-wise data are extracted along the center horizontal line.

Scheme	L^1 error	L^2 error	L^∞ error
Second-order GKS	1.802e0	4.452e0	1.249e1
Compact GKS	1.286e0	3.574e0	1.154e1

5.9. Sedov blast wave

As a standard benchmark for the Lagrangian method [33,47], the two dimensional Sedov blast wave is presented here to test the robustness of the scheme and its ability to capture the strong shocks. The computational domain $[0, 1.2] \times [0, 1.2]$ is covered by a uniform mesh with $100 \times 100 \times 2$ mesh points. A uniform distribution $(\rho, U, p) = (1, 0, 10^{-6})$ is given initially except in the cell on the upper left corner, which mimics a singular point at $(0, 1.2)$. In this cell, the pressure is set as $p = (\gamma - 1)\epsilon_0 / V$, where V is the cell area and $\epsilon_0 = 0.244816$ is the total internal energy. The symmetric boundary is given for the left and top boundaries, and the non-reflection boundary condition is set for the right and top ones. The
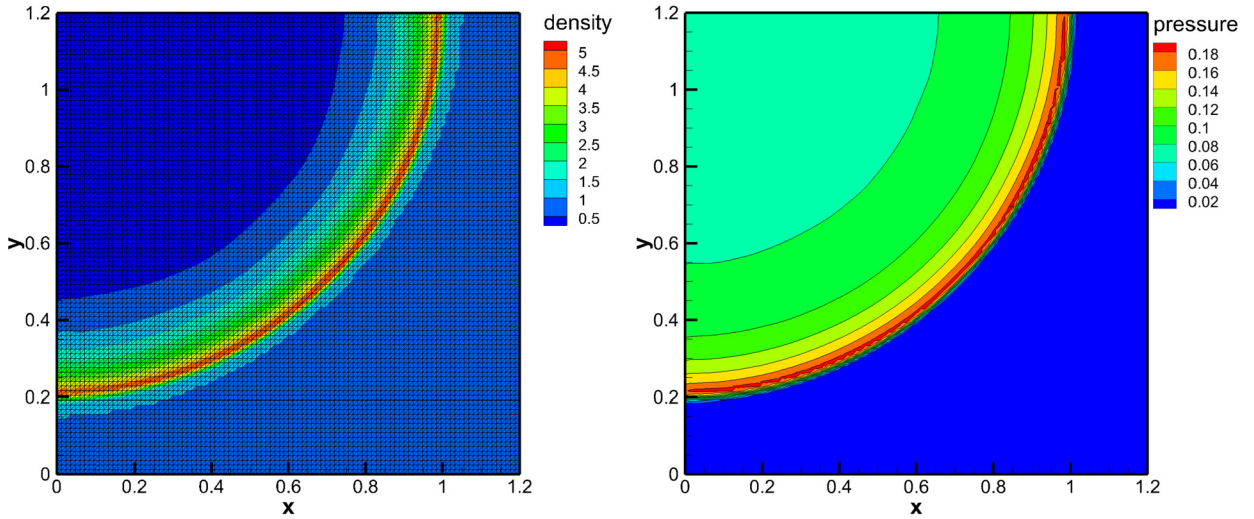
Fig. 16. Sedov blast wave: the density and pressure distributions at $t = 1$ with $100 \times 100 \times 2$ cells.
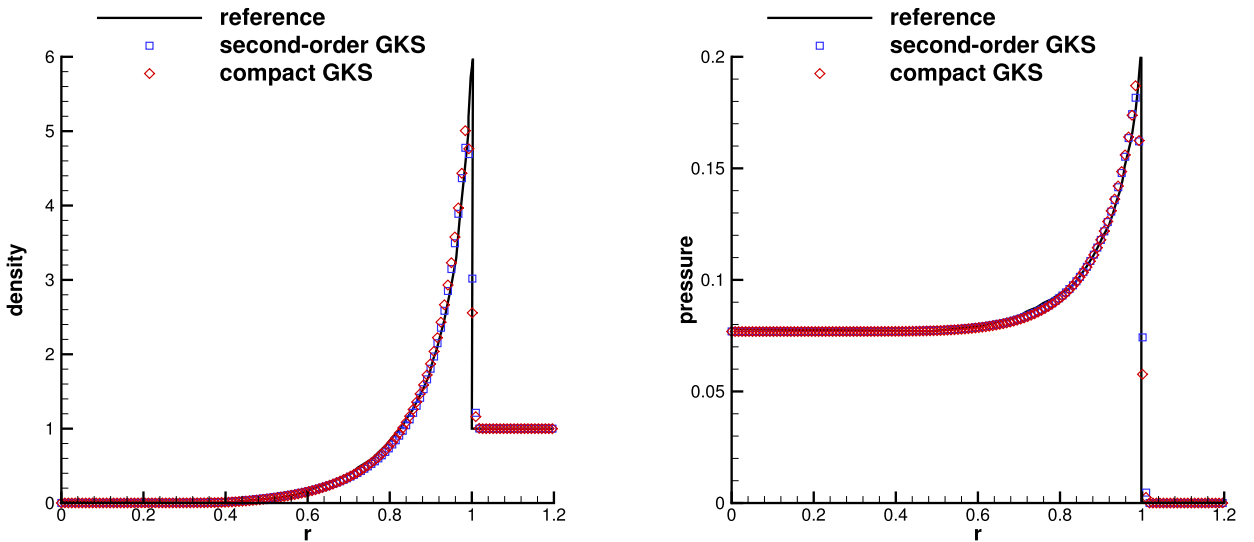
Fig. 17. Sedov blast wave: the density and pressure distributions of different schemes along the diagonal line at $t = 1$.

flow distributions are plotted at $t = 1$ in Fig. 16. The location of the numerical shock front agrees well with the analytical solution, which is located at $r = 1$ from the singular point. The density and pressure data are extracted along the diagonal line, as shown in Fig. 17. The high peak can be resolved by the compact scheme better than the second-order one. The GKS in arbitrary Lagrangian-Eulerian formulation can give a much improved solution even with a coarser mesh [42].

5.10. Shock-vortex interaction

The interaction between a vortex and a stationary shock for the inviscid flow [27] is presented. The computational domain is $[0, 1.5] \times [0, 1]$. A stationary Mach 1.1 shock is positioned at $x = 0.5$ and normal to the x-axis. The mean flow on the left is $(\rho, U, V, p) = (Ma^2, \sqrt{\gamma}, 0, 1)$, where Ma is the Mach number. A circular vortex is designed by a perturbation on the mean flow field with the velocity (U, V), temperature $T = p/\rho$, and entropy $S = \ln(p/\rho^{\gamma})$. The perturbation is expressed as

$$(\delta U, \delta V) = \kappa \eta e^{\mu(1-\eta^2)}(\sin\theta, -\cos\theta),$$

$$\delta T = -\frac{(\gamma - 1)\kappa^2}{4\mu\gamma} e^{2\mu(1-\eta^2)}, \delta S = 0,$$
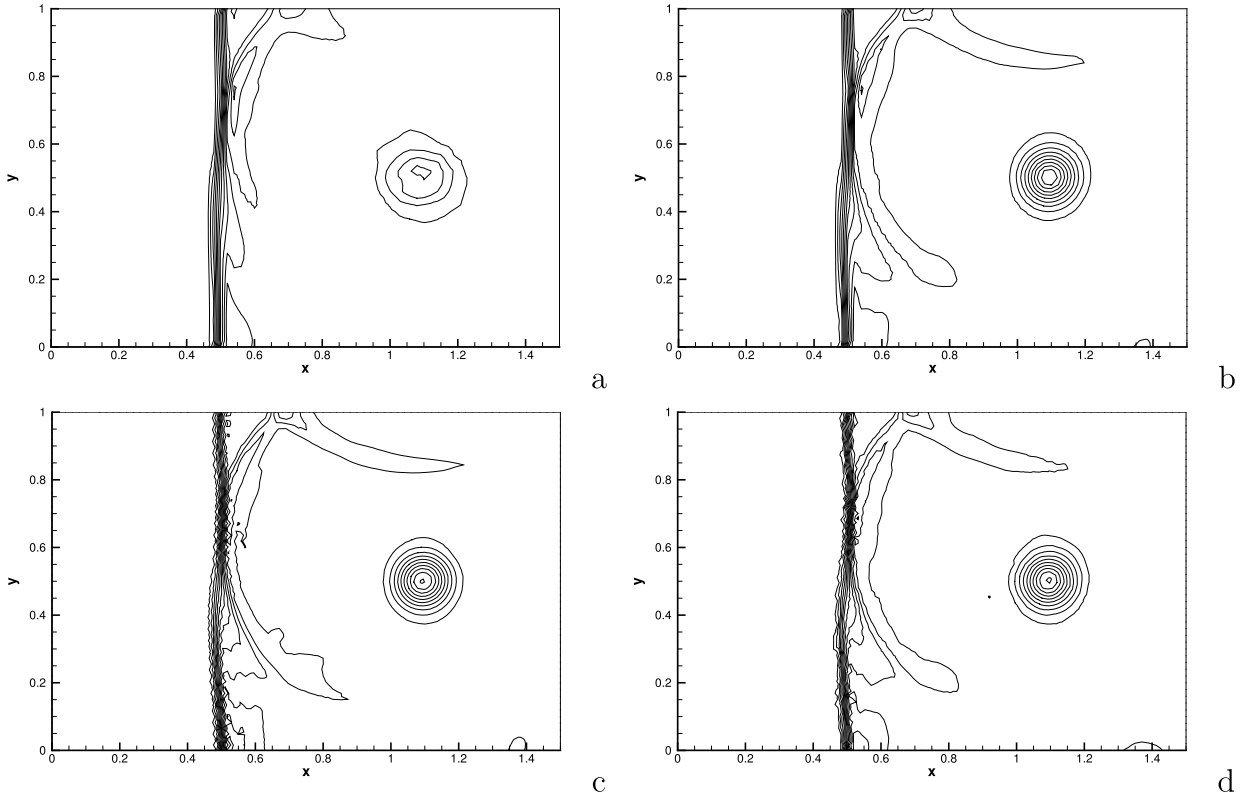
Fig. 18. Shock-vortex interaction: density contours obtained under uniform mesh by a second-order GKS (a), and uniform mesh, regular mesh and irregular mesh by current compact scheme (b,c,d) at $t = 0.8$ with $h = 1/50$.

where $\eta = r/r_c$, $r = \sqrt{(x - x_c)^2 + (y - y_c)^2}$, and $(x_c, y_c) = (0.25, 0.5)$ is the center of the vortex. Here κ represents the vortex strength, μ controls the decay rate of the vortex, and r_c is the critical radius where the vortex reaches the maximum strength. In current computation, $\kappa = 0.3$, $\mu = 0.204$, and $r_c = 0.05$. The reflected boundary conditions are used on the top and bottom boundaries. Inflow and outflow boundary conditions are applied along the entrance and exit. The numerical results by the current scheme under a coarse mesh are compared with traditional second-order GKS in Fig. 18. The density and pressure distributions along the center horizontal line with meshes $h = 1/50, 1/100, 1/200$ at $t = 0.8$ are compared in Fig. 19. The peak values around $x = 1.1$ are well resolved under all three types of triangular meshes with $h = 1/50$.

5.11. Forward step problem

This standard test case is originally from [53] for inviscid flow. Initially, a Mach 3 flow is moving from left to right in a wind tunnel. The computational domain is a rectangle with 3 unit long and 1 unit wide. The mesh is shown in Fig. 20. The walls of the tunnel are set as reflective boundary conditions. The inflow boundary condition is set at the left entrance while the outflow boundary condition is set at the right exit. In the computation, the mesh near the corner is refined to $h = 1/240$ to minimize flow separation from this singular corner. The results with $h = 1/60, 1/120, 1/240$ at $t = 4$ are presented in Fig. 21. The instability along the slip line starting from the triple point can be clearly observed with a rather coarse mesh of $h = 1/120$.

5.12. Double Mach reflection problem

We now consider the double Mach reflection problem [53] for the inviscid flow. The computational domain is shown in Fig. 22. Initially a right-moving Mach 10 shock is positioned at $(x, y) = (0, 0)$, and reflected by a 30° wedge. The initial pre-shock and post-shock conditions are

$$(\rho, U, V, p) = (8, 4.125\sqrt{3}, -4.125, 116.5),$$
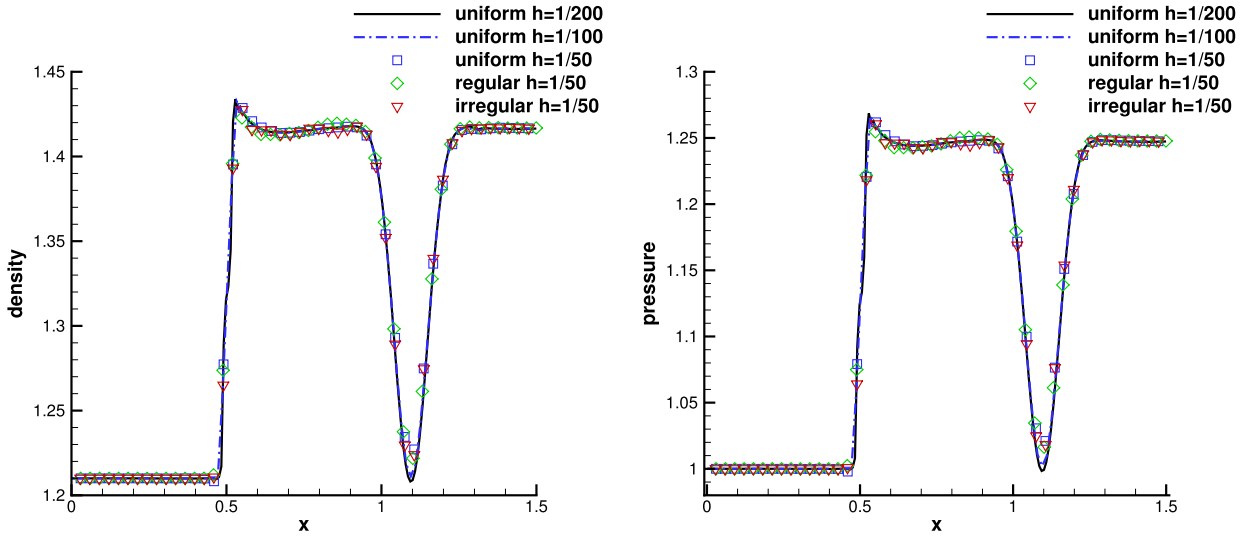
$$(\rho, U, V, p) = (1.4, 0, 0, 1).$$

Fig. 19. Shock-vortex interaction: density and pressure distributions along the center horizontal line under different meshes at $t = 0.8$.
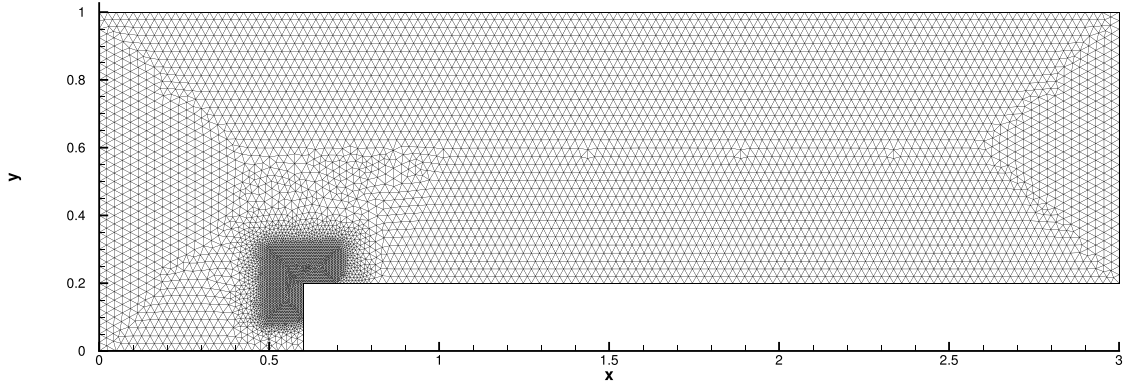

Fig. 20. Mach 3 forward step problem: mesh sample with $h = 1/40$.

The reflecting boundary condition is used along the wedge. The exact post-shock condition is imposed for the rest of the bottom boundary. The flow variables are set to follow the motion of the shock at the top boundary. The inflow boundary condition and the outflow boundary condition are set accordingly at the entrance and the exit. The density distributions and the local enlargements with $h = 1/160$ and $1/320$ at $t = 0.2$ are shown in Fig. 23. The robustness of the compact GKS is validated, while the flow structure around the slip line from the triple Mach point is resolved nicely by the compact scheme.

5.13. Lid-driven cavity flow

The lid-driven cavity problem is one of the most important benchmarks for validating incompressible or low-speed Navier-Stokes flow solvers. The fluid is bounded in a unit square and is driven by a uniform translation of the top boundary. In this case, the flow is simulated with Mach number $Ma = 0.15$ and all boundaries are isothermal and nonslip. The computational domain is $[0, 1] \times [0, 1]$. As presented in Fig. 24, the domain is covered by $35 \times 35 \times 2$ mesh points. The stretching rate is 1.15 with the minimum mesh size $h \approx 0.007$ near the wall boundary. Numerical simulations are obtained at three different Reynolds numbers, i.e., $Re = 400$, $Re = 1000$, and 3200. The streamlines for $Re = 1000$ are shown in Fig. 24. The U-velocity along the center vertical line, and V-velocity along the center horizontal line, are shown in Fig. 25. The benchmark data [16] at the corresponding Reynolds numbers are also presented, and the simulation results match well with these benchmark solutions.

5.14. Laminar boundary layer

A low-speed laminar boundary layer with incoming Mach number $Ma = 0.15$ is simulated over a flat plate with Reynolds number $Re = U_\infty L/\nu = 10^5$, where $L = 100$ is the characteristic length. The computational domain is shown in Fig. 26,
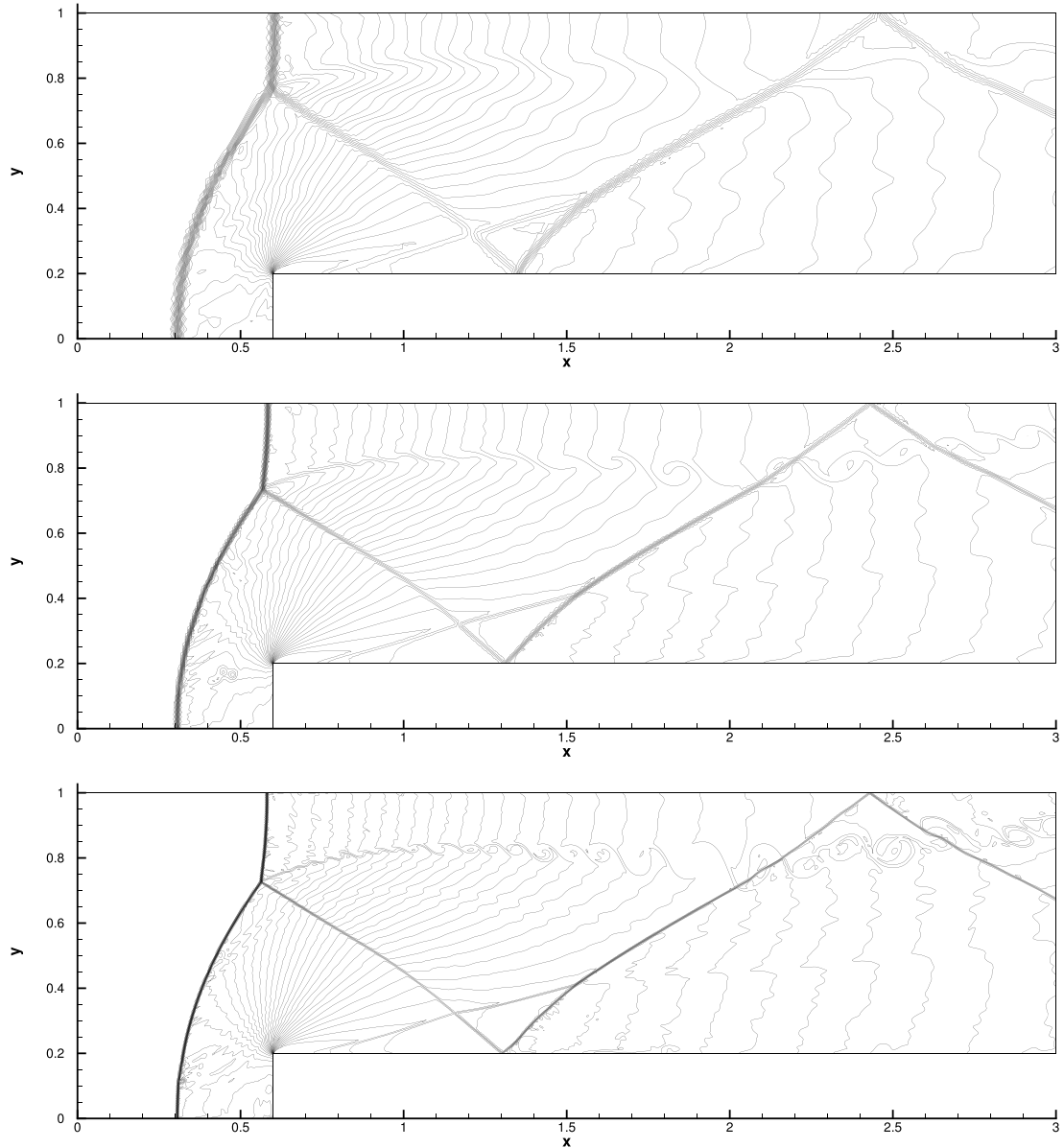
Fig. 21. Mach 3 forward step problem: density distributions on different meshes with $h = 1/60$, $1/120$, $1/240$ at $t = 4$. 30 contours are used.

where the flat plate is placed at $x > 0$ and $y = 0$. Total $75 \times 47 \times 2$ mesh points are used in the domain with a refined cell size $h = 0.05$ close to the boundary. The mesh is generated from $(0, 0)$ with a stretching ratio of 1.1 along the positive x-direction, 1.3 along the negative x-direction, and 1.1 along the positive y-direction. There are 20 mesh points in the front of the plate. Adiabatic non-slip boundary condition is imposed on the plate and symmetric slip boundary condition is set at the bottom boundary in the front of the plate. The non-reflecting boundary condition based on the Riemann invariants is adopted for the other boundaries, where the free stream is set as $\rho_\infty = 1$, $p_\infty = 1/\gamma$. The non-dimensional velocity U and V are given in Fig. 27 at four selected locations. The numerical results match well with the analytical solutions even with a few mesh points at $x/L = 0.0525$.

5.15. Hypersonic flow around a cylinder

In this case, both inviscid and viscous hypersonic flows impinging on a cylinder are tested to validate the robustness of the current scheme.
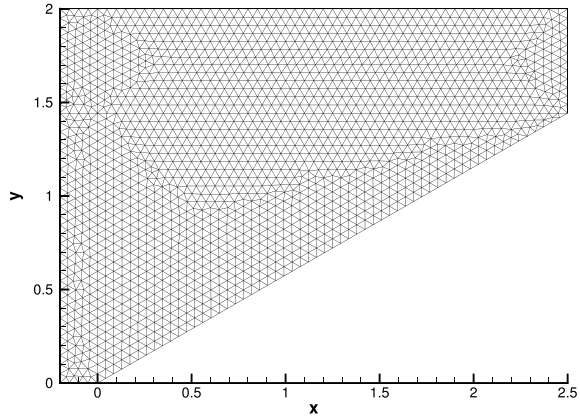
Fig. 22. Double Mach reflection problem: Mesh distribution with $h = 1/20$.
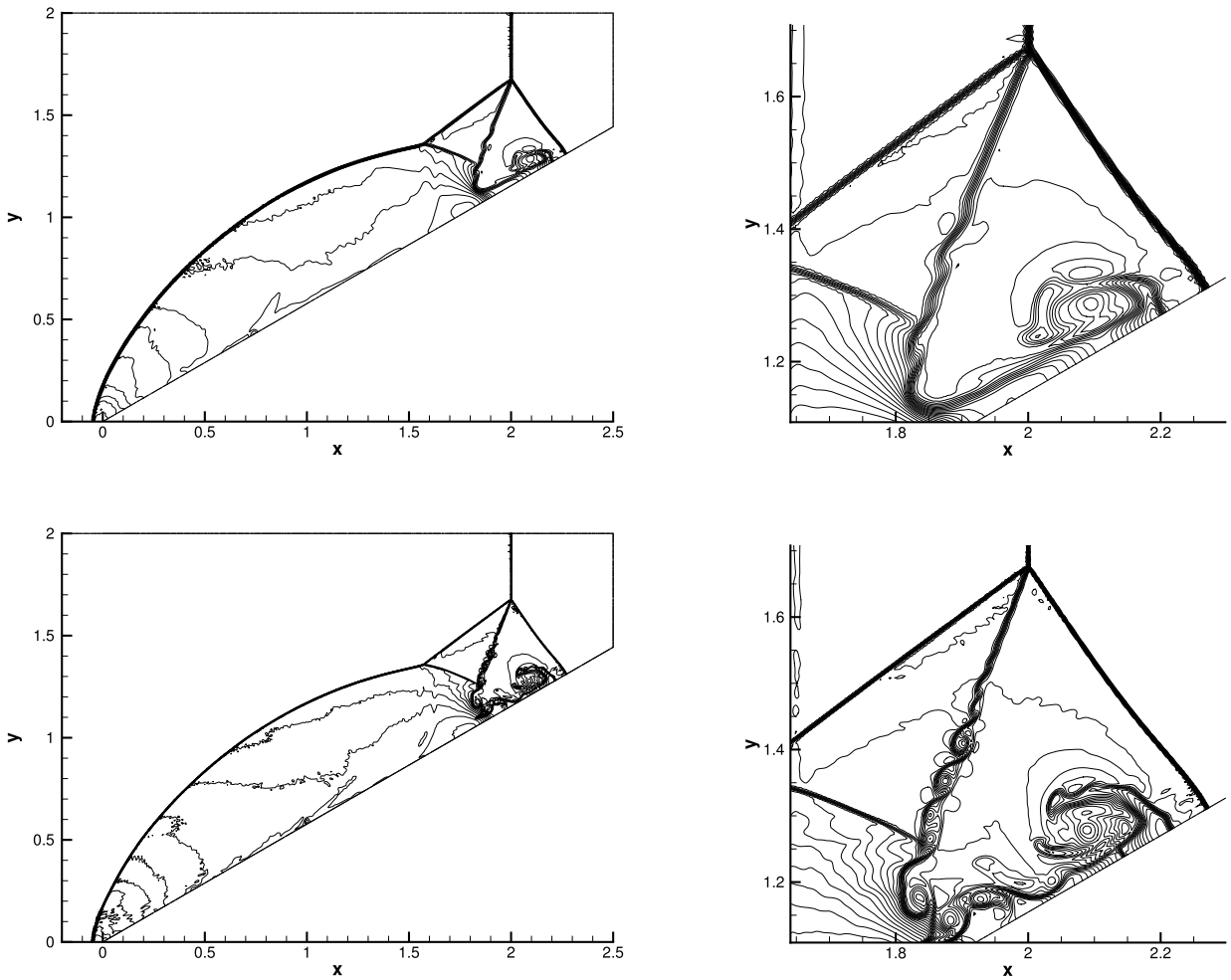
Fig. 23. Double Mach reflection problem: density distributions and zoomed-in pictures around the Mach stem under non-uniform-mesh at $t = 0.2$ with $h = 1/160$, $1/320$. 30 contours are used.
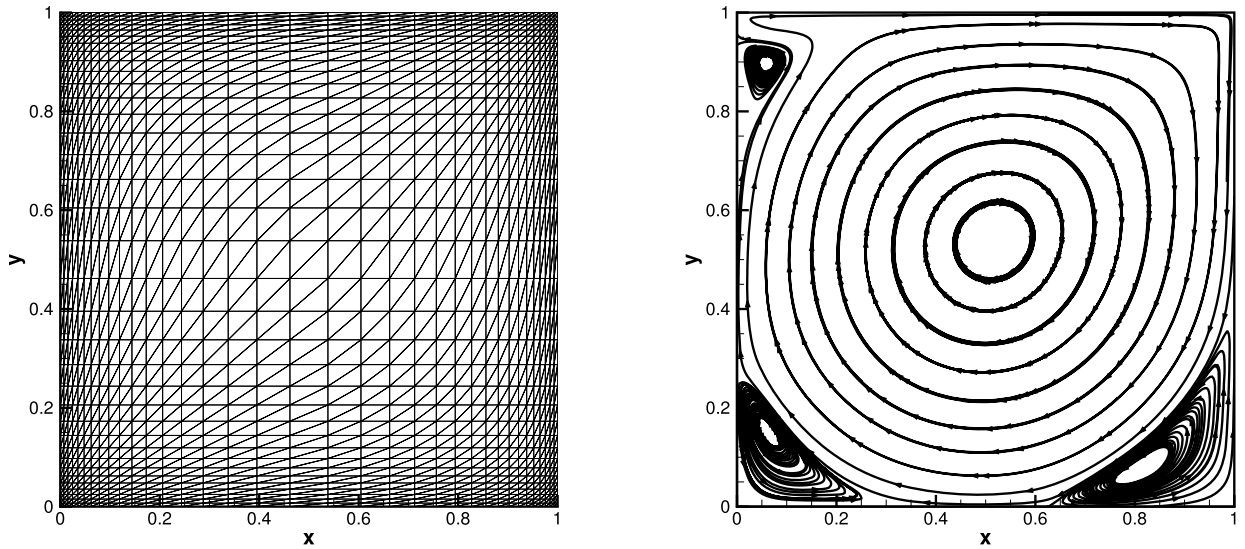
Fig. 24. Lid-driven cavity flow. Left: mesh $35 \times 35 \times 2$ with $\Delta h \approx 0.007$ near the solid wall. Right: the stream line under $Re = 3200$ case.

(a) Inviscid Cases

The first one is for the Euler solutions. The incoming flow has Mach numbers up to 20 on the cylinder. The reflective boundary condition is imposed on the wall of the cylinder while the right boundary is set as outflow boundary condition. Firstly, a uniform quadrilateral mesh with 60 cells along radial direction and 50 cells along circumferential direction is split diagonally in each cell for triangulation which is used in the computation. The mesh size along radial direction is 0.03. The uniform mesh and Mach number distributions are presented in Fig. 28. The results agree well with those performed under structured mesh by the original non-compact high order GKS [41]. To further demonstrate the robustness of the compact scheme, an irregular mesh with near-wall thickness $h \approx 0.03$ is used for this case as well. Under such a mesh at Mach number 20, the limiter on the HWENO weights is triggered to avoid the appearance of negative temperature. The mesh and flow distributions are plotted in Fig. 29. In all cases with different triangular mesh, the current compact scheme can capture strong shocks very well without the carbuncle phenomenon. The robustness of the scheme is fully validated.

(b) Viscous Case

This test is taken from the experiment by Wieting [52]. The non-slip isothermal boundary condition with wall temperature $T_w = 294.44K$ is imposed as the cylinder surface. The far-field flow condition is given by $Ma_\infty = 8.03$, $T_\infty = 124.94K$. The Reynolds number is $Re = 1.835 \times 10^5$. Two meshes named as Mesh I and Mesh II are used for this test case. As shown in Fig. 30, to resolve the boundary layer Mesh I is generated by simple triangulation of a non-uniform quadrilateral mesh of 80×161 points with a near-wall thickness $h \approx 10^{-4}$ and a stretching ratio 1.1. As an explicit scheme, the CFL number is set as 0.1 due to the stiffness of the viscous term. To improve the efficiency, a primary flow field calculated by the first-order kinetic method [54] is used as the initial field. The pressure and Mach number distributions are given in Fig. 30. The non-dimensional pressure and heat flux along the cylindrical surface are extracted and shown in Fig. 31. Generally, the numerical results agree well with the experiment data [52]. The heat flux is calculated by the Fourier's law through the temperature gradient on the wall. To show the capacity of mesh adaptability for the current scheme, Mesh II with high non-uniformity in the bow shock region is used, which is shown in Fig. 32. In the near-boundary region, the mesh size starts from $h \approx 10^{-5}$ and grows up to 80 layers with a stretching ratio of 1.1. 61 mesh points are used along the circumferential direction. The numerical results agree well with the experimental data with Mesh II, as shown in Fig. 33.

6. Conclusion

In this paper, a two-stage compact GKS has been developed on unstructured triangular mesh. Different from the first-order Riemann solver, the GKS provides a time-accurate solution through the evolution of gas distribution function at a cell interface. Besides providing numerical fluxes and their time derivatives, the explicit time evolution solution also updates the flow variables at the cell interface, which can be used to get the averaged gradients of flow variables inside each triangular mesh through the Green-Gauss theorem. As a result, a third-order GKS has been constructed with compact reconstruction based on cell averaged flow variables and their gradients and MSMD time stepping technique for the two-stage third-order accuracy. Even with the same stencils as other compact schemes, the current GKS distinguishes it from the original HWENO [43] and DG [9] methods in the ways of gradients updates. In the DG formulation, the gradient inside each control volume is directly evaluated at the next time level through a weak formulation. As a result, the CFL number used in GKS can be much larger than that in the same order DG method. With the implementation of a modified HWENO reconstruction, the
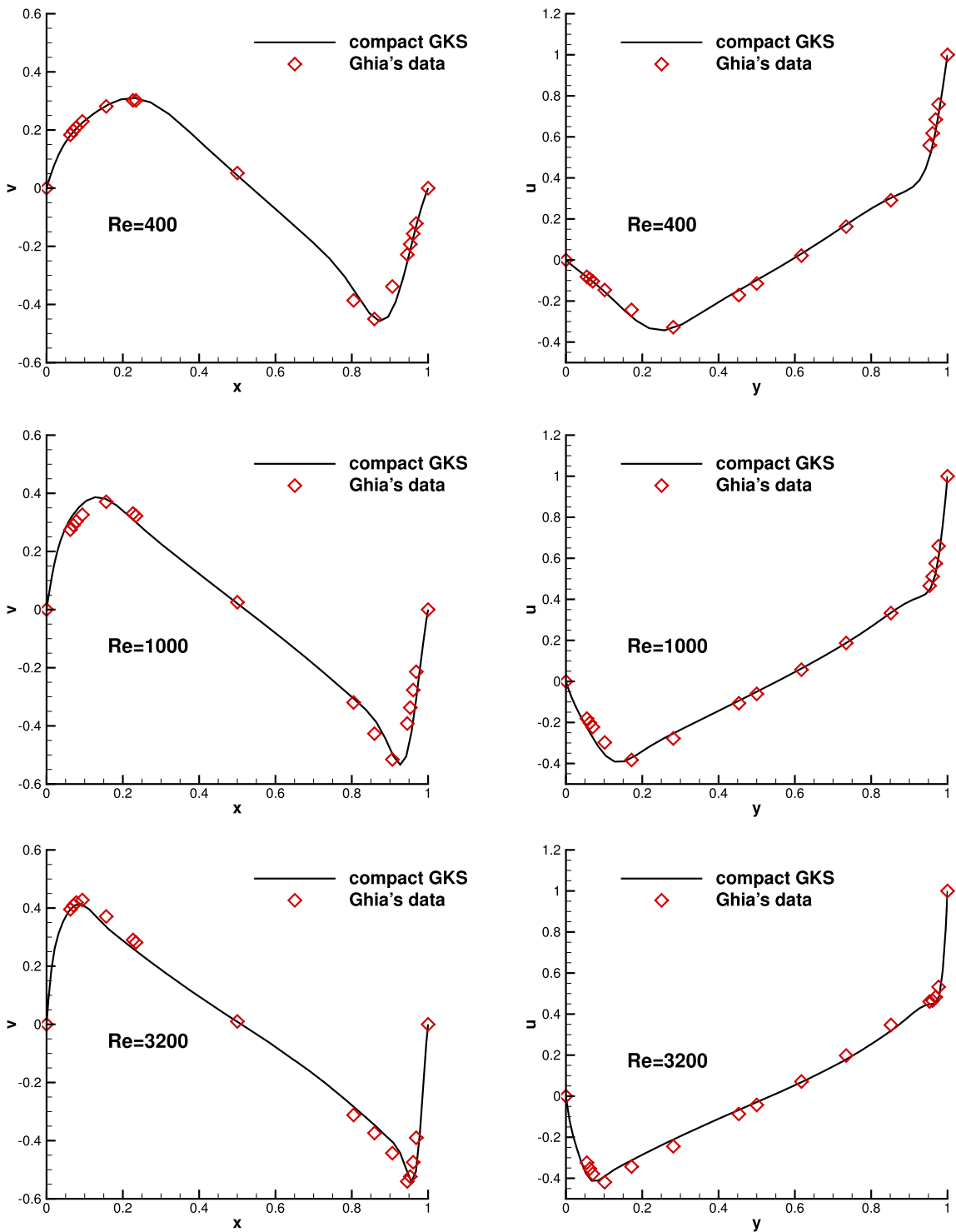
Fig. 25. Lid-driven cavity flow. V-velocities along the horizontal centerline and U-velocities along the vertical centerline with $Re = 400, 1000, 3200$ (from top to bottom).
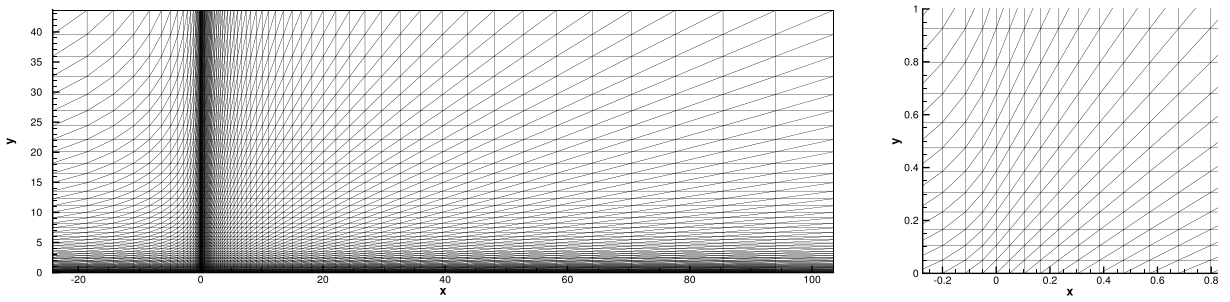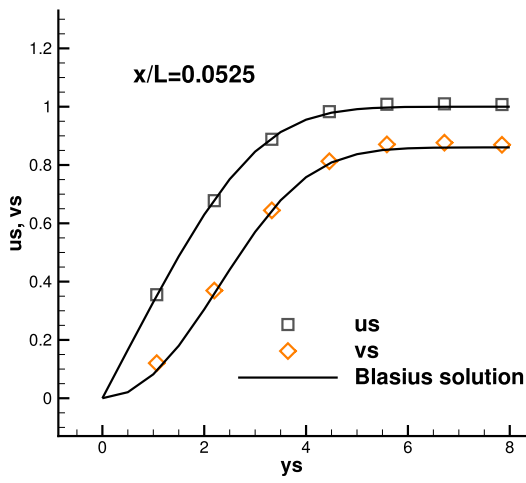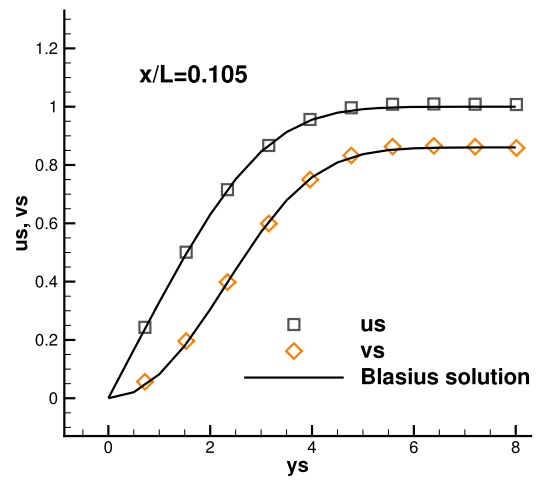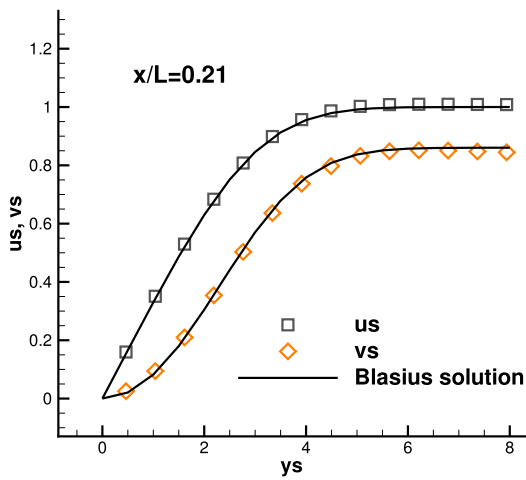
Fig. 26. Computational domain for laminar boundary layer. $75 \times 47 \times 2$ mesh points are used with a wall thickness $h = 0.05$ in the front of the flat plate.
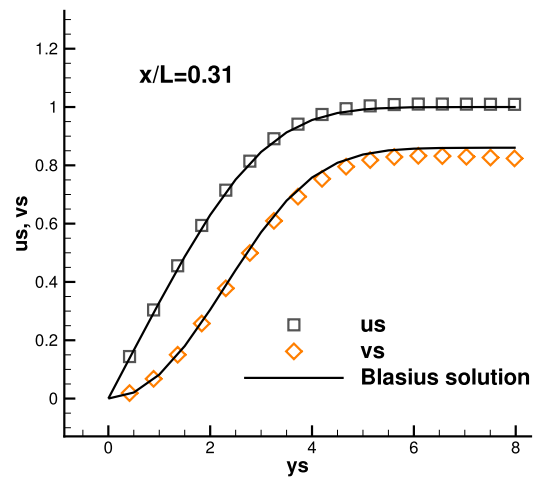

(a) $x/L = 0.0525$

(b) $x/L = 0.105$

(c) $x/L = 0.21$

(d) $x/L = 0.31$

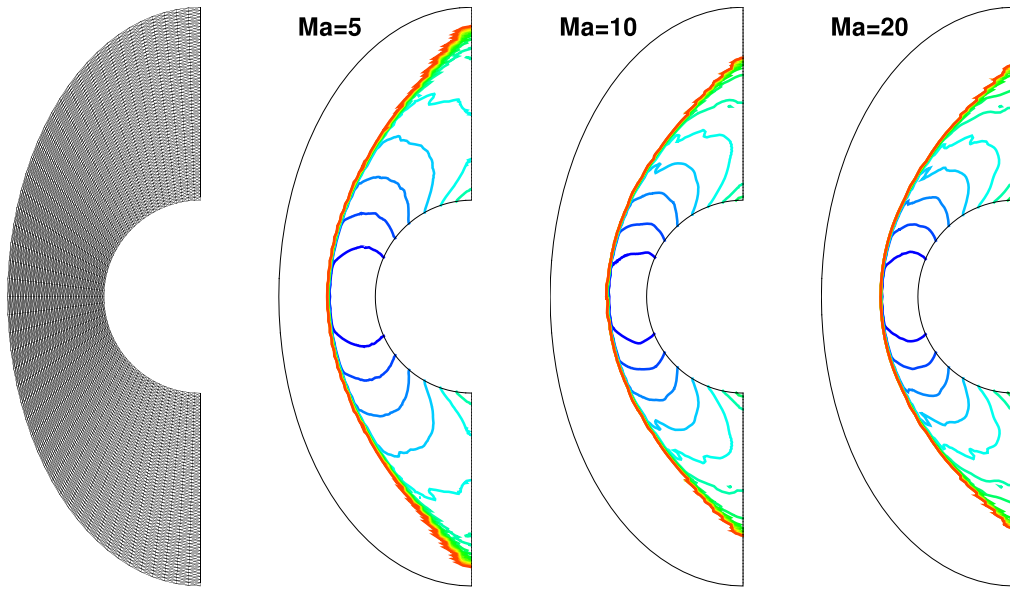**Fig. 27.** Laminar boundary layer: the non-dimensional velocity profile at different locations.

Fig. 28. Hypersonic inviscid flow passing through a circular cylinder: Mach number distributions with Mach number $Ma = 5, 10$, and 20 under uniform mesh. CFL $= 0.4$.
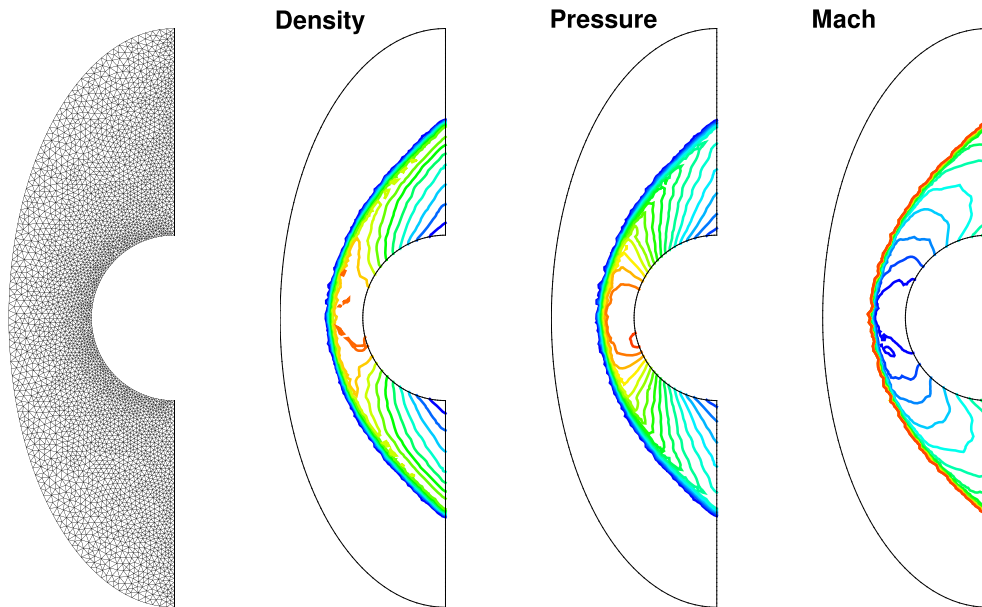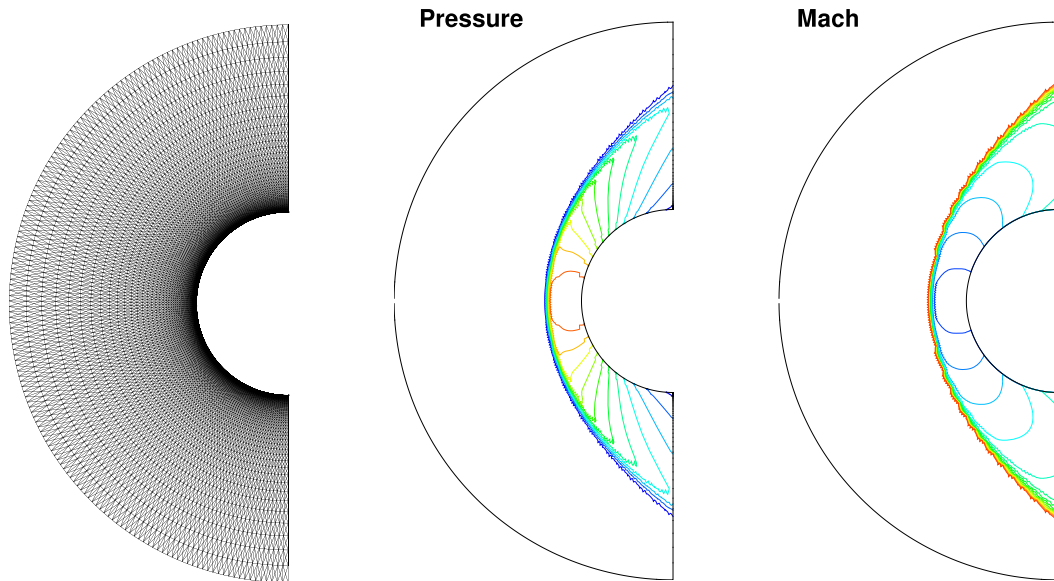

Fig. 29. Hypersonic inviscid flow passing through a circular cylinder: mesh, density, pressure, and Mach number distributions by the compact third-order GKS. Mach $= 20$, CFL $= 0.2$.

current third-order compact GKS has the same robustness as the second-order shock capturing scheme. There is no trouble cell detection in all test cases in this paper. Only under extreme condition, such as Mach 20 flow passing through a cylinder with unfavorable irregular mesh, a limiting technique on the HWENO reconstruction weights is triggered. The proposed scheme shows good mesh adaptivity even for a highly irregular triangular mesh. In the previous compact GKS method, all pointwise values at Gaussian points of a cell interface are used directly to get an over-determined system in the quadratic polynomial reconstruction. The use of cell averaged gradients in the current scheme reduces the stiff connectivity in flow variables between cells. As a result, the current compact GKS with direct application of HWENO reconstruction becomes more robust and accurate than the previous method on unstructured mesh. The compact GKS can resolve vortices better than that from the third-order non-compact finite volume methods in [64]. The extension of the current compact scheme to even higher-order accuracy is under investigation.

Fig. 30. A Mach number 8.03 viscous flow passing through a circular cylinder with Mesh I: mesh, pressure, and Mach number distributions by the compact third-order GKS. CFL = 0.1. The mesh size near the wall is $h \approx 10^{-4}$.
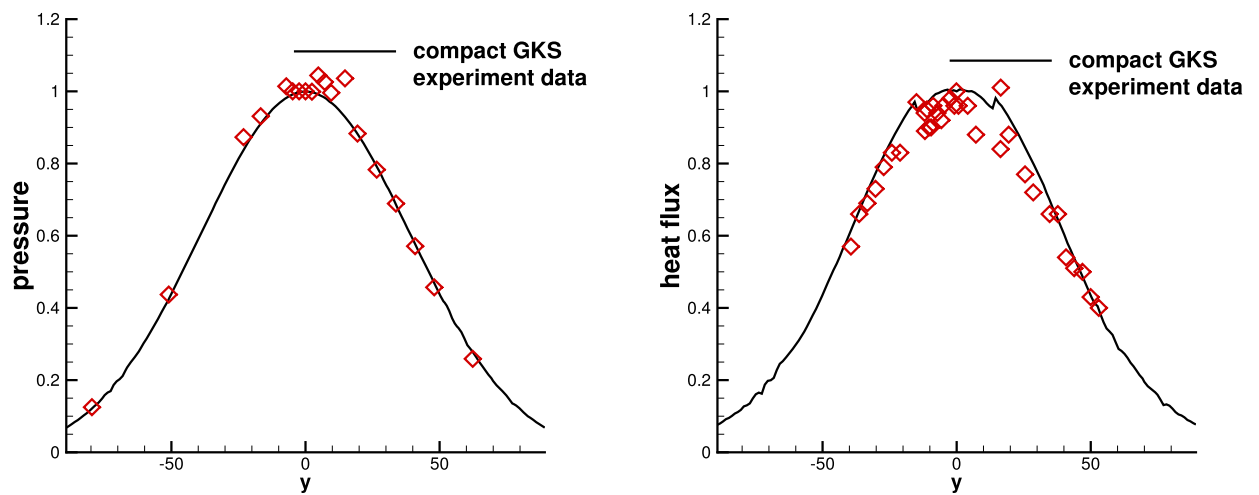
Fig. 31. A Mach number 8.03 viscous flow passing through a circular cylinder with Mesh I: non-dimensional pressure and heat flux distributions along the surface of cylinder which are compared with the experimental data in [52].
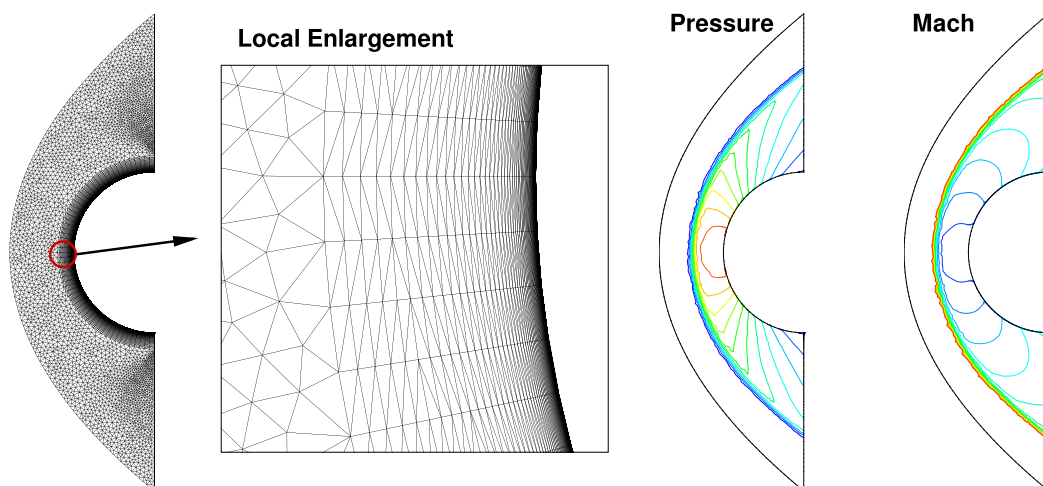
Declaration of competing interest

The authors declare that they have no known competing financial interests or personal relationships that could have appeared to influence the work reported in this paper.
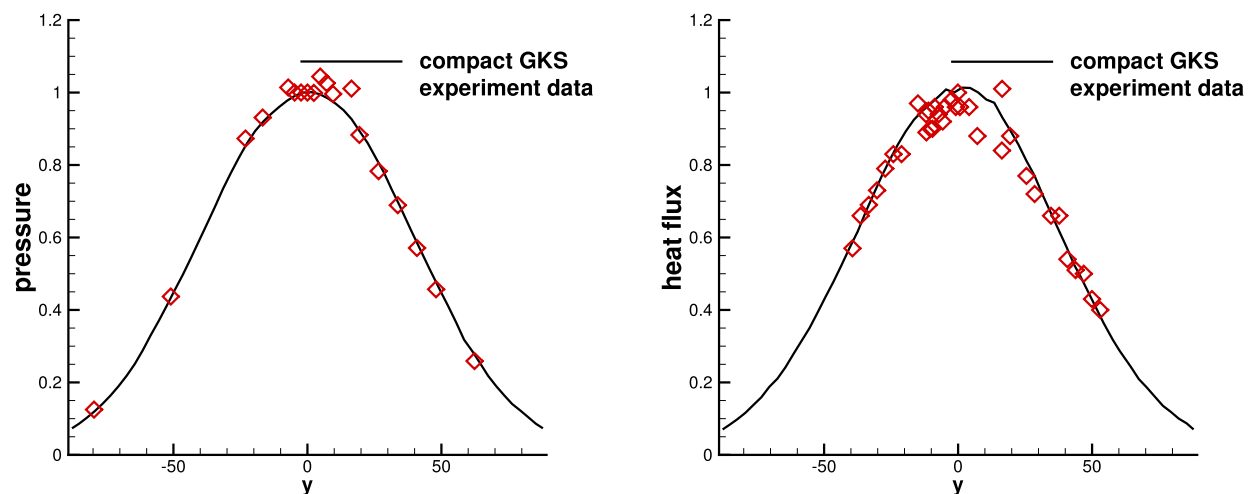
The authors declare that they have no known conflict of interest in this paper.

Acknowledgement

Fig. 32. A Mach number 8.03 viscous flow passing through a circular cylinder with Mesh II: mesh, pressure, and Mach number distributions by the compact third-order GKS. CFL = 0.1. The mesh size near the wall is $h \approx 10^{-5}$.

Fig. 33. A Mach number 8.03 viscous flow passing through a circular cylinder with Mesh II: non-dimensional pressure and heat flux distributions along the surface of cylinder which are compared with the experimental data in [52].

References

[1] P.L. Bhatnagar, E.P. Gross, M. Krook, A model for collision processes in gases. I. Small amplitude processes in charged and neutral one-component systems, Phys. Rev. 94 (3) (1954) 511.

[2] R. Borges, M. Carmona, B. Costa, W.S. Don, An improved weighted essentially non-oscillatory scheme for hyperbolic conservation laws, J. Comput. Phys. 227 (6) (2008) 3191–3211.

[3] G. Cao, H. Liu, K. Xu, Physical modeling and numerical studies of three-dimensional non-equilibrium multi-temperature flows, Phys. Fluids 30 (12) (2018) 126104.

[4] G. Cao, L. Pan, K. Xu, Three dimensional high-order gas-kinetic scheme for supersonic isotropic turbulence I: criterion for direct numerical simulation, Comput. Fluids 192 (2019) 104273.

[5] R.P. Chan, A.Y. Tsai, On explicit two-derivative Runge-Kutta methods, Numer. Algorithms 53 (2) (2010) 171–194.

[6] J. Cheng, Z. Du, X. Lei, Y. Wang, J. Li, A two-stage fourth-order discontinuous Galerkin method based on the GRP solver for the compressible Euler equations, Comput. Fluids 181 (2019) 248–258.

[7] A.J. Christlieb, S. Gottlieb, Z. Grant, D.C. Seal, Explicit strong stability preserving multistage two-derivative time-stepping schemes, J. Sci. Comput. 68 (3) (2016) 914–942.

[8] B. Cockburn, S. Hou, C.-W. Shu, The Runge-Kutta local projection discontinuous Galerkin finite element method for conservation laws. IV. The multidimensional case, Math. Comput. 54 (190) (1990) 545–581.

[9] B. Cockburn, C.-W. Shu, TVB Runge-Kutta local projection discontinuous Galerkin finite element method for conservation laws. II. General framework, Math. Comput. 52 (186) (1989) 411–435.

[10] B. Cockburn, C.-W. Shu, Runge–Kutta discontinuous Galerkin methods for convection-dominated problems, J. Sci. Comput. 16 (3) (2001) 173–261.

[11] Z. Du, J. Li, A Hermite WENO reconstruction for fourth order temporal accurate schemes based on the GRP solver for hyperbolic conservation laws, J. Comput. Phys. 355 (2018) 385–396.

[12] M. Dumbser, Arbitrary high order PNPM schemes on unstructured meshes for the compressible Navier–Stokes equations, Comput. Fluids 39 (1) (2010) 60–76.

[13] M. Dumbser, D.S. Balsara, E.F. Toro, C.-D. Munz, A unified framework for the construction of one-step finite volume and discontinuous Galerkin schemes on unstructured meshes, J. Comput. Phys. 227 (18) (2008) 8209–8253.

[14] E. Fehlberg, Low-Order Classical Runge-Kutta Formulas with Stepsize Control and Their Application to Some Heat Transfer Problems, 1969.

[15] C. Geuzaine, J.-F. Remacle, Gmsh: a 3-D finite element mesh generator with built-in pre-and post-processing facilities, Int. J. Numer. Methods Eng. 79 (11) (2009) 1309–1331.

[16] U. Ghia, K.N. Ghia, C. Shin, High-Re solutions for incompressible flow using the Navier-Stokes equations and a multigrid method, J. Comput. Phys. 48 (3) (1982) 387–411.

[17] S. Gottlieb, On high order strong stability preserving Runge–Kutta and multi step time discretizations, J. Sci. Comput. 25 (1) (2005) 105–128.

[18] S. Gottlieb, C.-W. Shu, E. Tadmor, Strong stability-preserving high-order time discretization methods, SIAM Rev. 43 (1) (2001) 89–112.

[19] Z. Grant, S. Gottlieb, D.C. Seal, A strong stability preserving analysis for explicit multistage two-derivative time-stepping schemes based on Taylor series conditions, Commun. Appl. Math. Comput. 1 (1) (2019) 21–59.

[20] E. Hairer, G. Wanner, Multistep-multistage-multiderivative methods for ordinary differential equations, Computing 11 (3) (1973) 287–303.

[21] C. Hu, C.-W. Shu, Weighted essentially non-oscillatory schemes on triangular meshes, J. Comput. Phys. 150 (1) (1999) 97–127.

[22] X.Y. Hu, N.A. Adams, C.-W. Shu, Positivity-preserving method for high-order conservative schemes solving compressible Euler equations, J. Comput. Phys. 242 (2013) 169–180.

[23] A. Jaust, J. Schütz, D.C. Seal, Implicit multistage two-derivative discontinuous Galerkin schemes for viscous conservation laws, J. Sci. Comput. 69 (2) (2016) 866–891.

[24] X. Ji, L. Pan, W. Shyy, K. Xu, A compact fourth-order gas-kinetic scheme for the Euler and Navier-Stokes equations, J. Comput. Phys. 372 (2018) 446–472.

[25] X. Ji, K. Xu, Performance enhancement for high-order gas-kinetic scheme based on WENO-adaptive-order reconstruction, arXiv preprint arXiv:1905.08489, 2019.

[26] X. Ji, F. Zhao, W. Shyy, K. Xu, A family of high-order gas-kinetic schemes and its comparison with Riemann solver based high-order methods, J. Comput. Phys. 356 (2018) 150–173.

[27] G.-S. Jiang, C.-W. Shu, Efficient implementation of weighted ENO schemes, J. Comput. Phys. 126 (1) (1996) 202–228.

[28] L. Krivodonova, M. Berger, High-order accurate implementation of solid wall boundary conditions in curved geometries, J. Comput. Phys. 211 (2) (2006) 492–512.

[29] D. Levy, G. Puppo, G. Russo, Central WENO schemes for hyperbolic systems of conservation laws, ESAIM: Math. Model. Numer. Anal. 33 (3) (1999) 547–571.

[30] J. Li, Z. Du, A two-stage fourth order time-accurate discretization for Lax–Wendroff type flow solvers I. Hyperbolic conservation laws, SIAM J. Sci. Comput. 38 (5) (2016) A3046–A3069.

[31] Q. Li, K. Xu, S. Fu, A high-order gas-kinetic Navier–Stokes flow solver, J. Comput. Phys. 229 (19) (2010) 6715–6731.

[32] R. Liska, B. Wendroff, Comparison of several difference schemes on 1D and 2D test problems for the Euler equations, SIAM J. Sci. Comput. 25 (3) (2003) 995–1017.

[33] R. Loubère, M.J. Shashkov, A subcell remapping method on staggered polygonal grids for arbitrary-Lagrangian–Eulerian methods, J. Comput. Phys. 209 (1) (2005) 105–138.

[34] H. Luo, J.D. Baum, R. Löhner, On the computation of steady-state compressible flows using a discontinuous Galerkin method, Int. J. Numer. Methods Eng. 73 (5) (2008) 597–623.

[35] H. Luo, L. Luo, R. Nourgaliev, V.A. Mousseau, N. Dinh, A reconstructed discontinuous Galerkin method for the compressible Navier–Stokes equations on arbitrary grids, J. Comput. Phys. 229 (19) (2010) 6961–6978.

[36] H. Luo, L. Luo, K. Xu, A BGK-based discontinuous Galerkin method for the Navier-Stokes equations on arbitrary grids, in: Computational Fluid Dynamics Review 2010, World Scientific, 2010, pp. 103–122.

[37] L. Pan, J. Cheng, S. Wang, K. Xu, A two-stage fourth-order gas-kinetic scheme for compressible multicomponent flows, Commun. Comput. Phys. 22 (4) (2017) 1123–1149.

[38] L. Pan, J. Li, K. Xu, A few benchmark test cases for higher-order Euler solvers, Numer. Math., Theory Methods Appl. 10 (4) (2017) 711–736.

[39] L. Pan, K. Xu, A third-order compact gas-kinetic scheme on unstructured meshes for compressible Navier–Stokes solutions, J. Comput. Phys. 318 (2016) 327–348.

[40] L. Pan, K. Xu, Two-stage fourth-order gas-kinetic scheme for three-dimensional Euler and Navier-Stokes solutions, Int. J. Comput. Fluid Dyn. 32 (2018) 395–411.

[41] L. Pan, K. Xu, Q. Li, J. Li, An efficient and accurate two-stage fourth-order gas-kinetic scheme for the Euler and Navier–Stokes equations, J. Comput. Phys. 326 (2016) 197–221.

[42] L. Pan, F. Zhao, K. Xu, High-order ALE gas-kinetic scheme with unstructured WENO reconstruction, arXiv preprint arXiv:1905.07837, 2019.

[43] J. Qiu, C.-W. Shu, Hermite WENO schemes and their application as limiters for Runge–Kutta discontinuous Galerkin method: one-dimensional case, J. Comput. Phys. 193 (1) (2004) 115–135.

[44] J. Schütz, D.C. Seal, A. Jaust, Implicit multiderivative collocation solvers for linear partial differential equations with discontinuous Galerkin spatial discretizations, J. Sci. Comput. 73 (2017) 1145–1163.

[45] D.C. Seal, Y. Güçlü, A.J. Christlieb, High-order multiderivative time integrators for hyperbolic conservation laws, J. Sci. Comput. 60 (1) (2014) 101–140.

[46] C.-W. Shu, S. Osher, Efficient implementation of essentially non-oscillatory shock-capturing schemes, II, in: Upwind and High-Resolution Schemes, Springer, 1989, pp. 328–374.

[47] H. Tang, T. Liu, A note on the conservative schemes for the Euler equations, J. Comput. Phys. 218 (2) (2006) 451–459.

[48] V. Titarev, E. Toro, Analysis of ADER and ADER-WAF schemes, IMA J. Numer. Anal. 27 (3) (2006) 616–630.

[49] Q. Wang, Y.-X. Ren, W. Li, Compact high order finite volume method on unstructured grids II: extension to two-dimensional Euler equations, J. Comput. Phys. 314 (2016) 883–908.

[50] R. Wang, R.J. Spiteri, Linear instability of the fifth-order WENO method, SIAM J. Numer. Anal. 45 (5) (2007) 1871–1901.

[51] Z. Wang, K. Fidkowski, R. Abgrall, F. Bassi, D. Caraeni, A. Cary, H. Deconinck, R. Hartmann, K. Hillewaert, H.T. Huynh, et al., High-order CFD methods: current status and perspective, Int. J. Numer. Methods Fluids 72 (8) (2013) 811–845.

[52] A. Wieting, M. Holden, Experimental study of shock wave interference heating on a cylindrical leading edge at Mach 6 and 8, in: 22nd Thermophysics Conference, 1987, p. 1511.

[53] P. Woodward, P. Colella, The numerical simulation of two-dimensional fluid flow with strong shocks, J. Comput. Phys. 54 (1) (1984) 115–173.

[54] K. Xu, Gas-kinetic schemes for unsteady compressible flow simulations, Lect. Ser. - Kareman Inst. Fluid Dyn. 3 (1998) C1–C202.

[55] K. Xu, A gas-kinetic BGK scheme for the Navier–Stokes equations and its connection with artificial dissipation and Godunov method, J. Comput. Phys. 171 (1) (2001) 289–335.

[56] K. Xu, Direct Modeling for Computational Fluid Dynamics: Construction and Application of Unified Gas-Kinetic Schemes, World Scientific, 2014.

[57] K. Xu, C. Liu, A paradigm for modeling and computation of gas dynamics, Phys. Fluids 29 (2) (2017) 026101.

[58] K. Xu, M. Mao, L. Tang, A multidimensional gas-kinetic BGK scheme for hypersonic viscous flow, J. Comput. Phys. 203 (2) (2005) 405–421.
[59] M. Yu, Z. Wang, Y. Liu, On the accuracy and efficiency of discontinuous Galerkin, spectral difference and correction procedure via reconstruction methods, J. Comput. Phys. 259 (2014) 70–95.
[60] C. Zhang, Q. Li, S. Fu, Z. Wang, A third-order gas-kinetic CPR method for the Euler and Navier–Stokes equations on triangular meshes, J. Comput. Phys. 363 (2018) 329–353.
[61] F. Zhao, X. Ji, W. Shyy, K. Xu, Compact higher-order gas-kinetic schemes with spectral-like resolution for compressible flow simulations, Adv. Aerodyn. 1 (1) (2019) 13.
[62] F. Zhao, L. Pan, S. Wang, Weighted essentially non-oscillatory scheme on unstructured quadrilateral and triangular meshes for hyperbolic conservation laws, Journal of Computational Physics 374 (2018) 605–624.
[63] J. Zhu, J. Qiu, Hermite WENO schemes and their application as limiters for Runge-Kutta discontinuous Galerkin method, III: unstructured meshes, J. Sci. Comput. 39 (2) (2009) 293–321.
[64] J. Zhu, J. Qiu, New finite volume weighted essentially nonoscillatory schemes on triangular meshes, SIAM J. Sci. Comput. 40 (2) (2018) A903–A928.